In situ investigation of neutrals involved in the formation of Titan tholins

David Dubois, Nathalie Carrasco, Marie Petrucciani, Ludovic Vettier, Sarah
Tigrine, Pascal Pernot

1   In situ Investigation of Neutrals Involved in the Formation of Titan Tholins

2

3

4   David Dubois[1], Nathalie Carrasco[1,2], Marie Petrucciani[1], Ludovic Vettier[1], Sarah Tigrine[1,3],

5   Pascal Pernot[4]

6

7

8

9   [1] LATMOS Laboratoire Atmosphères, Milieux et Observations Spatiales, Université Versailles

10   St-Quentin, 78280 Guyancourt, France

11   [2] Institut Universitaire de France, Paris F-75005, France

12   [3] Synchrotron SOLEIL, l'Orme des Merisiers, St Aubin, BP 48, 91192 Gif-sur-Yvette Cedex,
13   France
14   [4] Laboratoire de Chimie Physique, UMR 8000, CNRS, Université Paris-Sud 11, 91405, Orsay,

15   France

16

17

18

19

20

21

22

23   Revised

24   Pages: 46

25   Figures: 8

26   Tables: 2

27   Citations: 101

28

29   Supplementary Material

30   Pages: 9

31   Figures: 3

32   Tables: 3

33

34 **Abstract**

35

36 The Cassini Mission has greatly improved our understanding of the dynamics and chemical
37 processes occurring in Titan's atmosphere. It has also provided us with more insight into the
38 formation of the aerosols in the upper atmospheric layers.
39 However, the chemical composition and mechanisms leading to their formation were out of
40 reach for the instruments onboard Cassini. In this context, it is deemed necessary to apply and
41 exploit laboratory simulations to better understand the chemical reactivity occurring in the gas
42 phase of Titan-like conditions. In the present work, we report gas phase results obtained from a
43 plasma discharge simulating the chemical processes in Titan's ionosphere. We use the
44 PAMPRE cold dusty plasma experiment with an N_2-CH_4 gaseous mixture under controlled
45 pressure and gas influx. An internal cryogenic trap has been developed to accumulate the gas
46 products during their production and facilitate their detection. The cryogenic trap condenses the
47 gas-phase precursors while they are forming, so that aerosols are no longer observed during
48 the 2h plasma discharge. We focus mainly on neutral products NH_3, HCN, C_2H_2 and C_2H_4. The
49 latter are identified and quantified by *in situ* mass spectrometry and infrared spectroscopy. We
50 present here results from this experiment with mixing ratios of 90-10% and 99-1% N_2-CH_4,
51 covering the range of methane concentrations encountered in Titan's ionosphere. We also
52 detect *in situ* heavy molecules (C_7). In particular, we show the role of ethylene and other
53 volatiles as key solid-phase precursors.

54

55 **Keywords:** Titan, Saturn; Atmospheres, chemistry; Plasma discharge; Experimental techniques

56

57

58

59

60

61

62

63

I) Introduction

Titan is Saturn's largest moon and second largest in the Solar System after Ganymede. It has a mean radius of 2,575 km. One major interest in Titan is its uniquely dense (a 1.5-bar ground pressure) and extensive (~1,500 km) atmosphere, primarily made of N_2 and CH_4. In fact, the extent of the atmosphere alone accounts for about 58% in size of Titan's radius. Titan's first flyby by Pioneer 11 (1979) revealed the moon as being a faint brownish dot orbiting Saturn. The subsequent Voyager 1 (1980), Voyager 2 (1981), Cassini (2004 - 2017) and Huygens (2005) spacecraft have uncovered physicochemical processes unique in the solar system occurring both in the atmosphere and surface. Early seminal studies (Khare and Sagan, 1973; Sagan, 1973; Hanel et al., 1981) showed that Titan's reducing atmosphere is also composed of complex and heavy organic molecules and aerosols, their laboratory analogous counterparts coined *tholins*. This chemistry is initiated at high altitudes and participates in the formation of solid organic particles (Khare et al., 1981; Waite et al., 2007, and Hörst, 2017 for a more recent and holistic review of Titan's atmospheric chemistry). At altitudes higher than 800 km, the atmosphere is under the influence of energy deposition such as solar harsh ultraviolet (VUV) radiation, solar X-rays, Saturn's magnetospheric energetic electrons and solar wind (Krasnopolsky, 2009; Sittler et al., 2009). Cosmic dust input is also thought to chemically interact with volatiles in the middle atmosphere (English et al., 1996; Frankland et al., 2016). To wit, Titan is presumably one of the most chemically complex bodies in the solar system. Some of the techniques used to better understand the processes occurring in Titan's atmosphere are detailed hereafter.

Earth-based observations of Titan have been one way to determine the atmospheric composition and structure, as well as surface and subsurface features. For example, direct monitoring of seasonal tropospheric clouds from Earth-based observations helped us infer their transient locations (Brown et al., 2002). Ground-based submillimeter observations were used to infer the stratospheric composition with for example, the determination of hydrogen cyanide (HCN) and acetonitrile (CH_3CN) mixing ratios (Tanguy et al., 1990; Bezard and Paubert, 1993; Hidayat et al., 1997), and with the rise of ground-based observation techniques such as the Atacama Large Millimeter Array (ALMA) (Cordiner et al., 2014a, 2014b; Molter et al., 2016; Serigano et al., 2016; Palmer et al., 2017). The use of other space-based telescopes such as the Infrared Space Observatory (ISO) and the Herschel Space Observatory has additionally

97   provided information on the stratospheric composition and neutral abundances (Coustenis et al.,
98   2003; Courtin et al., 2011; Rengel et al., 2014). Early on, atmospheric studies brought by the
99   Voyager 1 mission were able to identify several organic molecules (Hanel et al., 1981; Kunde et
100   al., 1981; Maguire et al., 1981). Later, the Cassini-Huygens (NASA/ESA) mission provided us
101   with a more precise atmospheric characterization of the composition (Teanby et al., 2012;
102   Vinatier et al., 2015; Coustenis et al., 2016), wind (Flasar et al., 2005; Achterberg et al., 2011)
103   and upper atmosphere thermal profiles (e.g. Snowden et al., 2013), while the Huygens lander
104   (ESA) was able to provide insight on the *in situ* composition (Israel et al., 2005) and optical
105   properties of the aerosols (Doose et al., 2016). Cassini's Composite Infrared Spectrometer
106   (CIRS) limb spectral imaging (Vinatier et al., 2009) examined the role of volatiles in Titan's
107   chemistry and atmospheric dynamics. Many hydrocarbons and nitriles were shown to have wide
108   latitudinal variations of vertical mixing ratios (sometimes contradicting Global Circulation
109   Models, e.g. de Kok et al., 2014), emphasizing the importance of understanding the complex
110   coupling between gas phase chemistry and global dynamics. Both polar enrichments of nitriles
111   (e.g. Teanby et al., 2009) as well as the presence of heavy ions (Crary et al., 2009; Wellbrock et
112   al., 2013; Desai et al., 2017) have also been suggested to participate in Titan's aerosol
113   production. Thus, ground- and space-based observations have and will be especially important
114   in the post-Cassini era (Nixon et al., 2016).

115

116   Photochemical models have been complementarily used to predict the thermal,
117   compositional and structural evolution of Titan's atmospheric column (e.g. Atreya et al., 1978;
118   Carrasco et al., 2007, 2008). Furthermore, these models offer us testable hypotheses for
119   experiments and predictions for chemical pathways leading to the formation of aerosols (e.g.
120   Waite et al., 2007; Yelle et al., 2010).

121

122   Lastly, experimental techniques have also been used to simulate Titan's atmospheric
123   conditions (Khare et al., 1984; Sagan and Thompson, 1984; Pintassilgo et al., 1999; Cable et
124   al., 2012; Carrasco et al., 2013; Sciamma-O'Brien et al., 2015, Tigrine et al., 2016; Hörst et al.,
125   2018) and determine chemical mechanisms that are otherwise out of Cassini's reach. A wide
126   range of laboratory simulations have been used to complementarily investigate Titan's
127   atmospheric chemistry and different energy inputs (see Cable et al., 2012 for a thorough review
128   of these experiments). Typically in our lab, plasma discharges (Szopa et al., 2006; Sciamma-
129   O'Brien et al., 2010; Carrasco et al., 2012) or UV irradiation (Peng et al., 2013) have been used
130   to achieve Titan-like ionospheric conditions. In this context, it is deemed necessary to apply and

131 exploit such a technique to better understand the chemical reactivity occurring in Titan-like
132 upper atmospheric conditions. Hence, the gas phase which we know is key to the formation of
133 aerosols on Titan (Waite et al., 2007) is emphasized. Indeed, chemical precursors that are
134 present in the gas phase (Carrasco et al., 2012) follow certain chemical pathways that still need
135 to be investigated. For instance, Sciamma-O'Brien et al., 2010 showed how the production of
136 atomic hydrogen coming from CH_4 was anti-correlated with aerosol formation, by changing the
137 initial methane amount in the discharge. They argued that the presence of molecular and atomic
138 hydrogen in too large amounts in the gas mixture may have an inhibiting effect on the
139 polymerization reaction that produce the tholins.
140 To simulate the methane mixing ratios and energy conditions present in Titan's ionosphere, we
141 used the PAMPRE cold dusty plasma experiment (Szopa et al., 2006) with an N_2-CH_4 gas
142 mixture under controlled gas influx and pressure. Cold plasma discharges have been shown to
143 faithfully simulate the electron energy distribution of magnetospheric electrons and protons, and
144 UV irradiation deposited at Titan's atmosphere within a range of ~ 10 eV – 5 keV (Sittler et al.,
145 1983; Chang et al., 1991; Maurice et al., 1996; Brown et al., 2009; Johnson et al., 2016),
146 making them good laboratory analogs to simulate the ionospheric chemistry.

148   A first study (Gautier et al., 2011) dealt with the identification of gas products in the
149 PAMPRE reactor and used an external cold trap to study the gas phase. Analyses were made
150 by gas-chromatography coupled to mass spectrometry. More than 30 reaction products were
151 detected and a semi-quantitative study was performed on nitriles, the most abundant molecules
152 collected. However, one of the limitations to this technique is how the products are transported
153 *ex situ*, and may allow for loss or bias in their chemical reactivity and measurements. *In situ*
154 detections were then made by mass spectrometry with no cryogenic trapping (Carrasco et al.,
155 2012). Unfortunately, the only use of mass spectrometry prevented any univocal identification of
156 large organic molecules likely involved as precursors for aerosol formation. Since then, setup
157 improvements such as an internal cryogenic trap and infrared spectroscopy have been made in
158 order to study the gas phase *in situ* using these different complementary techniques. The
159 purpose of the cryotrap is to act as a cold finger enabling the volatiles to condensate and
160 preventing them from being evacuated from the chamber. This has allowed us to avoid any
161 volatile loss and to take on a quantitative approach on volatile products. Thus, to better
162 characterize the initial volatile products precursors to aerosols, we used a coupled analysis of
163 mass and infrared spectrometry. The presence of an internal cold trap made the condensation
164 of these volatiles possible, allowing for *in situ* measurements.

165

166 We will first describe our experimental chamber, which was designed to be relevant to simulate

167 Titan's ionosphere conditions. This was achieved by choosing methane concentrations

168 pertaining to those found in the upper atmosphere. Mass spectrometry results of volatiles at two

169 methane concentrations will be then presented, as well as their infrared spectroscopic analyses

170 with a quantitative approach taken on four major neutral volatiles (NH_3, C_2H_2, C_2H_4 and HCN)

171 acting as precursors to the formation of aerosols. Finally, we will discuss the discrepancies

172 between both methane conditions, as well as ethylene, ammonia and hydrogen cyanide

173 chemistry.

174

175

176 **II) Experimental Setup**

177

178 ***2.1. The PAMPRE experiment and in situ cryogenic analysis***

179

180 The PAMPRE cold plasma reactor used in this study aims, by design, at reproducing

181 exogenic energy sources, for example Saturn's magnetosphere particles, UV radiation, cosmic

182 rays and coronal processes impacting Titan's atmosphere (Szopa et al., 2006; Alcouffe et al.,

183 2010). The reactor delivers a capacitively coupled plasma discharge, produced by a 13.56 MHz

184 radiofrequency generator through a tuning match box. The gas influx is held constant and

185 monitored with mass flow controllers. The latter can tune an N_2-CH_4 mixing ratio from 0% to

186 10% of CH_4 from highly pure N_2 (>99.999%) and 90-10% N_2-CH_4 (>99.999%) bottles. An *in situ*

187 mass spectrometer (MS) and Fourier-Transform Infrared (FT-IR) spectrometer are also

188 integrated to the system.

189 To simulate Titan's atmospheric conditions, 90-10% and 99-1% N_2-CH_4 ratios were considered.

190 Both correspond to a 55 sccm flow in standard conditions. Pressure gauges are set at 0.9 mbar

191 of constant pressure in the reactor while the plasma power is constant at 30W.

192

193 In order to detect, analyze and preserve all of the products during our experiments, we

194 need a trapping mechanism to capture these compounds, and thus prevent them from being

195 evacuated. Gautier et al. (2011) used an external cryogenic trap system, shaped as a cylindrical

196 coil, immersed in liquid nitrogen. Then, they isolated the coiled trap and analyzed the gas phase

197 *ex situ*. Here, the setup is different, and we believe more efficient as the trapping and

198 subsequent analyses are performed *in situ* and avoid any transfer line bias. Moreover, this

199 cryo-trap mainly traps the gas-phase chemistry in the preceding stages to the formation of solid
200 organic aerosols, preventing their production. In the absence of such a cryo-trap, the plasma is
201 dusty and several mg/h of solid particles are produced. As a result, this enables us to effectively
202 study in detail these gas-phase precursors of tholins, trapped and accumulated during a 2h
203 plasma discharge. Fig. 1 shows the 3D schematics of our cryogenic trap. An external liquid
204 nitrogen tank extends as a copper circuit into the chamber for cooling. This cooling circuit goes
205 through the upper lid of the chamber, and spirals down onto and lays flat on the polarized
206 electrode. This cooling system is semi-closed, in that the remaining liquid nitrogen is stored in
207 another container outside the reactor. The electrode temperature is controlled with a
208 temperature regulator (Cryo-Diffusion Pt100 probe) which controls the liquid nitrogen circulation
209 in the cooling circuit with a solenoid valve. The initial temperature is adjusted to -180 ±2ºC prior
210 to the experiment.
211
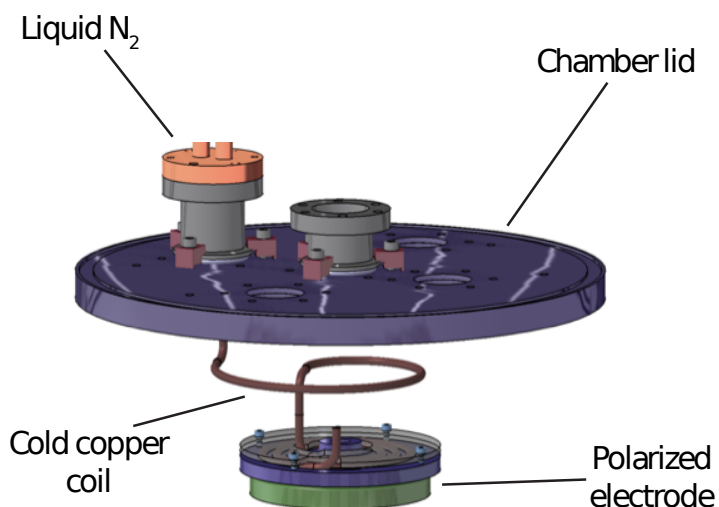
Fig. 1. 3D schematics of the cryogenic trap. The cold trap goes through the top lid of the reactor and coils down into the chamber, which is then in contact with the polarized electrode. The electrode is thus cooled to low-controlled temperatures and the liquid nitrogen goes out through an exit system. This cryogenic trap enables the *in situ* condensation of the produced volatiles within the plasma.

219   Using the cryogenic trap set at T = -180 ±2 ºC, the protocol used was the following: The plasma

220   discharge and cooling system are turned on and the electrodes are kept for 2h at T = -180ºC.

221   The duration of the plasma discharge was chosen to trap and accumulate the gas phase

222   products, and improve their detection. The discharge reaches a steady state after a few

223   minutes, as shown in Alcouffe et al., (2010). A similar 2h trapping was previously performed in

224   Gautier et al., (2011) with an external cold trap, which was then analyzed by GC-MS. For

225   consistency, we have chosen the same discharge duration. During this time, the products

226   formed in the N_2-CH_4 plasma are accumulated and adsorbed onto the chamber walls still at low-

227   controlled temperatures thanks to the cryogenic system. After 2h, the plasma is switched off, the

228   chamber is pumped down from 0.9 mbar to 10^{-4} mbar, and the cold trap is stopped. The volatile

229   products are gradually released under vacuum. We then proceed to do *in situ* gas phase

230   measurements as the chamber goes back to room temperature (Fig. 3). During this temperature

231   increase, it is possible that some additional neutral-neutral chemistry could occur. Our analytical

232   capacity enables us to address the most abundant and therefore stable molecules, which are

233   not expected to vary strongly apart from the sublimation process.

234

235   **2.2. Mass Spectrometry**

236

237   QMS quadrupole mass spectrometers were used (Pfeiffer and Hiden Analytics) for *in*

238   *situ* measurements inside the chamber. Once the neutral gas is ionized within the MS chamber

239   (SEM voltage of 1000V), each mass is collected by the detector. The MS samples near the

240   reactive plasma with a 0.8 mm-diameter capillary tube, long enough to keep a high-pressure

241   gradient between the MS and plasma chambers. Thus, an effective 10^{-5}-10^{-6} mbar resident

242   pressure in the MS chamber is maintained throughout the experiment. This vacuum background

243   was thoroughly checked before each simulation. The experiments were done using a 1u

244   resolution, covering a 1-100 mass range, at a speed of 2s/mass with a channeltron-type

245   detection. Finally, a baseline noise filter was applied to each spectrum.

246

247   **2.3. Infrared Spectroscopy**

248

249   A ThermoFisher Nicolet 6700 Fourier Transform Infrared (FT-IR) spectrometer was used

250   for *in situ* analysis of the gas phase in transmission mode. The spectrometer uses a Mercury

251   Cadmium Telluride (MCT/A) high sensitivity detector with a KBr beamsplitter. During each

252   measurement, 500 scans were taken at a resolution of 1 cm^{-1} for 650–4000 cm^{-1} corresponding

253   to a short-wavelength mid-IR (15.4–2.5 μm) range. The optical path length is 30 cm.

254

III) Results

255

256

257

258 We will now present results from two sets of experiments done at two initial methane
259 concentrations, 1% and 10% (three and two replicates, respectively), representative of the
260 methane concentration range found in Titan's ionosphere (Waite et al., 2005). The effect of the
261 cold trap on the plasma can be appreciated by comparing the mass spectra in the same
262 conditions with and without the cold trap (Fig. 2).

263
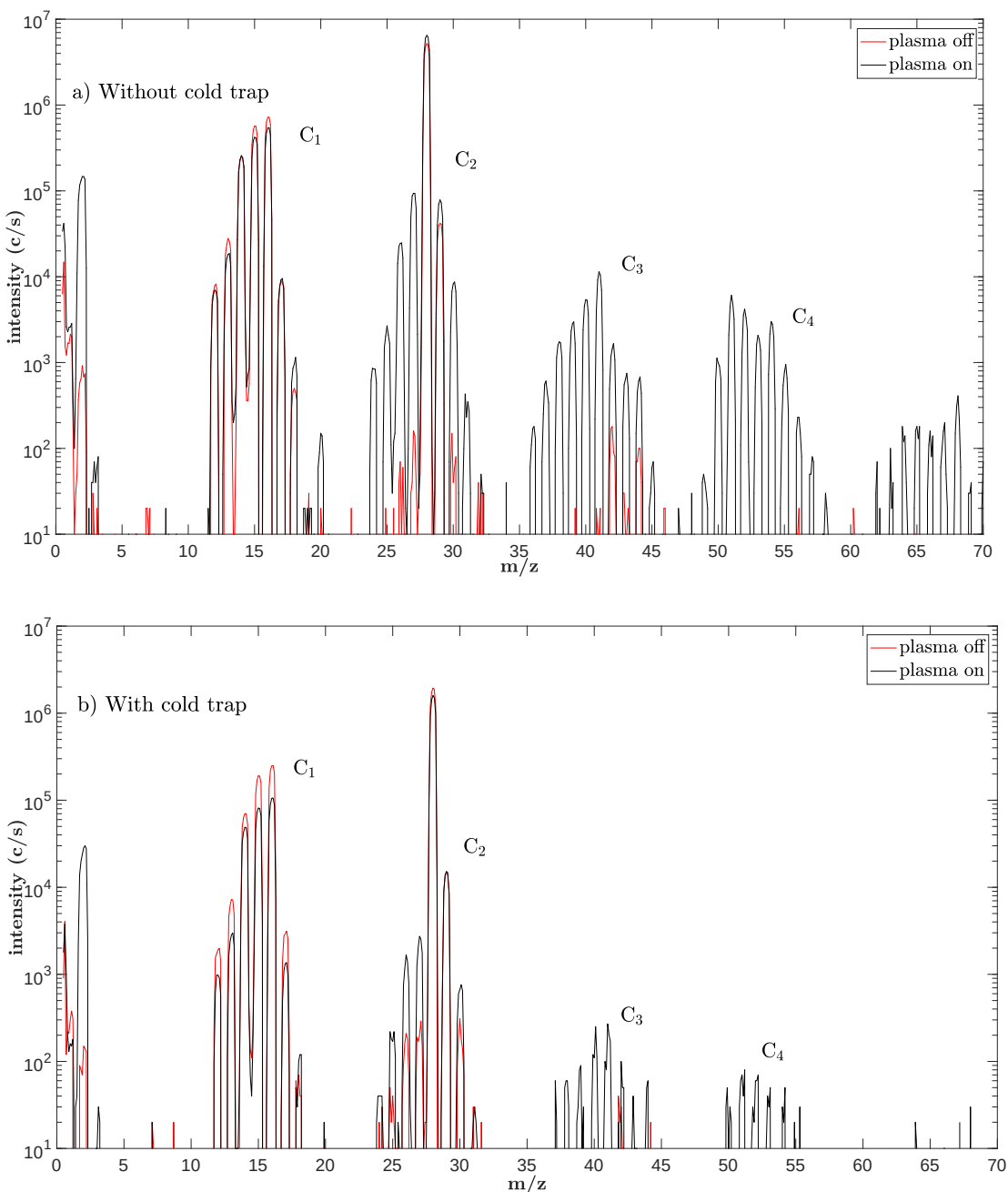
266   **Fig. 2.** (a) Upper panel: No cryogenic trap. Mass spectra of a 90-10% N_2-CH_4 mixture with plasma off (red) and
267   plasma on (black). The consumption of methane at m/z 16 and its fragments m/z 15, 13, 12 is visible after the plasma
268   is switched on. (b) Lower panel: With cold trap. Mass spectra of a 90-10% N_2-CH_4 mixture with plasma off (red) and
269   plasma on (black). The main products seen in the top plot (C_2, C_3 and C_4) decrease by about two orders of magnitude
270   in intensity in the bottom figure. This shows the efficient role of the cryotrap, which is to trap (albeit not completely
271   here) the gas products formed in the plasma.

272

273   Fig. 2 shows two sets of N_2-CH_4 mass spectra, one (in red) taken before the plasma is switched
274   on, the other (in black) taken 5 min after plasma ignition, thus making sure methane dissociation
275   and the plasma have reached their equilibrium state (Sciamma-O'Brien et al., 2010; Alves et al.,
276   2012).

277   The m/z 29 and 30 peaks are the isotopic signatures of N_2.
278   Under usual conditions, without cold-trap, several mg/h of solid particles are produced in the
279   plasma volume in steady state conditions after the very first minutes of the discharge (Sciamma-
280   O'Brien et al., 2010). Now, with the cold-trap, solid particles are no longer produced even after a
281   2h plasma duration: the aerosol formation is prevented. So, we must investigate how far the
282   gas-phase chemistry goes in the presence of the cold trap. The plasma is out of
283   thermodynamical equilibrium and hosts fast ion-neutral reactions. If the entrapment is faster
284   than the chemistry, then the absence of aerosols might be explained by the fact that any
285   product larger than CH_4 would be removed from the reaction space. But, if the chemical kinetics
286   of the gas phase chemistry is competitive with the entrapment, then complex molecules are
287   produced before their entrapment on the cold reactor walls. In this case, the absence of
288   aerosols is caused by the low amount of gas-phase precursors in the discharge, thus preventing
289   the gas-to-solid conversion. The analysis of the mass spectra obtained *in situ* during the plasma
290   discharge with and without cold-trap (Fig. 2) informs us on this effect of the cold-trap on the gas-
291   phase chemistry.

292

293   The methane consumption can be estimated with m/z 15 and m/z 16 on Fig. 2 corresponding to
294   the CH_3^+ and CH_4^+ fragments. Following the method described in Sciamma-O'Brien et al., 2010,
295   we quantify the methane consumption with the CH_3^+ (m/z 15) fragment at a pressure of 0.9
296   mbar. With the current cold trap setup, we found this consumption to be of 52% and 60% at
297   10% and 1% $[CH_4]_0$, respectively. Without the current cryotrap system, Sciamma-O'Brien et al.,
298   2010 found methane consumption efficiencies of 45% and 82% at 10% and 1% $[CH_4]_0$. The
299   behavior of methane consumption obtained with and without cold trap are comparable, even if
300   an effect of the different electrode temperature cannot be discarded.

301

302   In the following sections, we define C_n families as molecular classes using a $C_xH_yN_z$
303   nomenclature for N-bearing and hydrocarbon species, where $x + z = n$. As such, C_n blocks
304   detected using mass spectrometry can be traced, where *n* is related to the presence of heavy
305   aliphatic and N-bearing compounds.

306 In the C_1 block, in addition to the methane ion peaks, we can notice the signature of the residual
307 water of the mass spectrometer at m/z 17, 18. Other compounds due to the residual air in the
308 mass spectrometer can be seen at m/z 32 (O_2) and m/z 44 (CO_2).
309 The role of the cryotrap has a substantive effect on trapping organic volatile products. Heavy
310 compounds such as the C_4 block (Fig. 2a) vanish with the cold trap (Fig. 2b), despite similar
311 methane consumptions.
312 This shows the role of the cryo-trap, which is to efficiently condense and accumulate *in situ* the
313 organic products on the cold walls of the reactor instead of being evacuated out as volatiles
314 during the discharge.
315 Methane is consumed in similar quantities in the plasma discharge with and without the
316 cryotrap. Some large and complex molecules are still detected during the discharge by mass
317 spectrometry (Fig. 2b), up to the upper mass limits of our instrument (m/z 100) with the cold
318 trap, showing that the gas phase chemistry ensuring their formation is still occurring. Their
319 concentration in the gas phase is drastically reduced, by two orders of magnitude (Fig. 2b),
320 suggesting that they are efficiently trapped on the plasma walls while they are forming. The cold
321 trap does not prevent the formation of complex gas-phase molecules, but mainly blocks the gas-
322 to-solid conversion step. The cryogenic trap stops the gas-phase chemistry in the stage
323 preceding the formation of solid organic aerosols. It condenses the gas-phase precursors while
324 they are forming, and no aerosols are observed during the 2h plasma discharge.
325
326 **3.1 Release of volatiles back to room temperature**
327
328 We leave the cold trap continuously on during a 2h plasma discharge. After 2h, the plasma and
329 cryo-trap are stopped, the chamber is pumped down to 10^{-4} mbar, isolated, and left to go back
330 to room temperature. Hence, all the species condensed on the cold walls are progressively
331 desorbed according to their vaporization temperatures and analyzed *in situ*. We define MS1,
332 MS2 and MS3 (Figures 3 and 4) as three mass spectra for 10% $[CH_4]_0$ taken at three different
333 pressures (~ 0.38, 0.74 and 1.84 mbar) and temperatures (-130ºC, -79ºC and +22ºC) during
334 volatile release, respectively. The temperature heat-up rate initially increases relatively fast (~ 7
335 ºC/min between t = 0 min and the acquisition of the MS1 spectrum), then decreases to ~ 0.3
336 ºC/min near MS2 and finally reaches a temperature decrease rate of ~ 0.1 ºC/min above -50ºC
337 (MS3).
338 This desorption is recorded with a pressure gauge within the isolated chamber as the
339 temperature increases. Figure 3 (top) shows the pressure of the gas products being released

340 and the temperature of the electrode (bottom) according to time, both at $[CH_4]_0$ = 10% and

341 $[CH_4]_0$ = 1%, in blue and red, respectively. Both pressures increase, owing to the volatiles

342 sublimating though in different behaviors. Most of the volatiles have been released at ~6h of

343 release (Figure 3, top) and the curve starts to reach an asymptotic limit in the case of 10%

344 methane, (i) the release starts immediately with the temperature increase until 0.74 mbar at -

345 79ºC where it reaches a small plateau, followed by (ii) a second volatile release starting at -75ºC

346 with a sharp decrease in heating rate at 300 min until it (iii) reaches a second plateau at 1.84

347 mbar. On the other hand, products formed in $[CH_4]_0$ = 1% conditions have a different release

348 pattern. Notwithstanding the discrepancy in final pressure obtained (0.35 mbar, 5x less), the

349 products take a much longer time to be desorbed, the release starting at about 90 min with a

350 much smoother slope. Unlike at 10% methane, there is no plateau; the release of the volatiles is

351 continuous and in a rather limited pressure range.

352 These qualitative differences suggest, as a first approximation, different products in the two

353 methane conditions. In particular, all the products released at temperatures below -100ºC at

354 10% methane are absent in the case of 1% methane. This means that these specific

355 compounds are not produced in significant amounts in the plasma discharge at 1% CH_4.

356

357

358
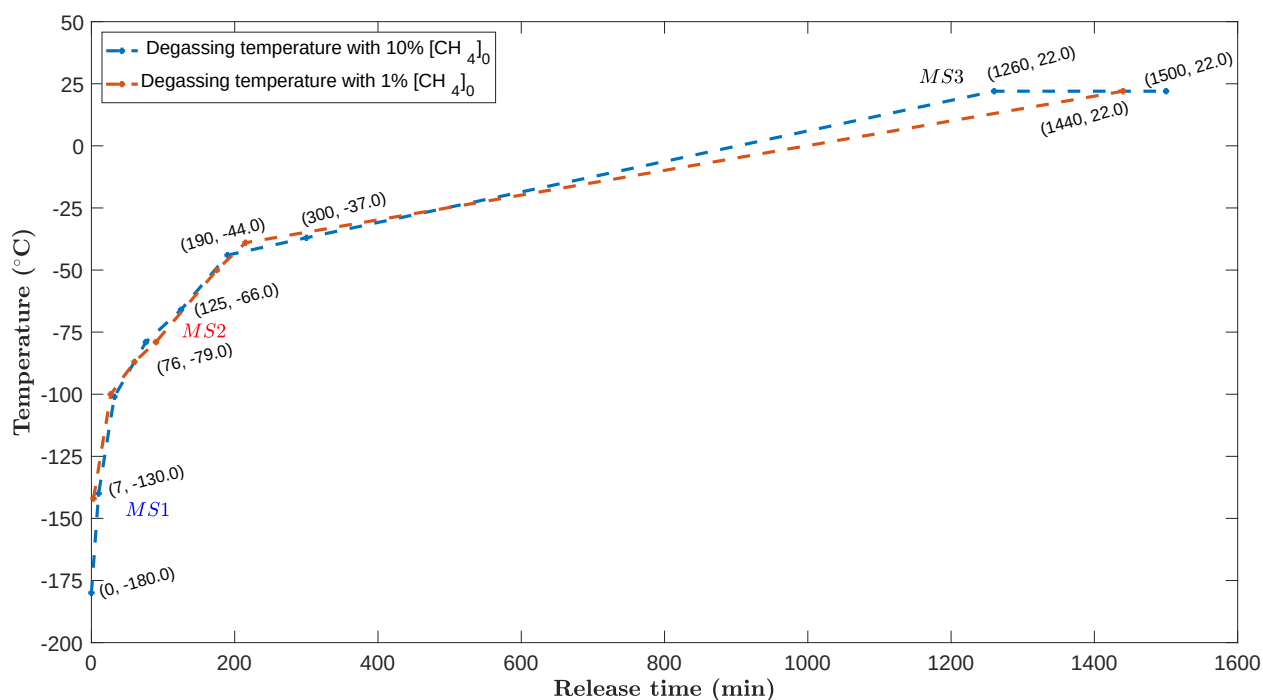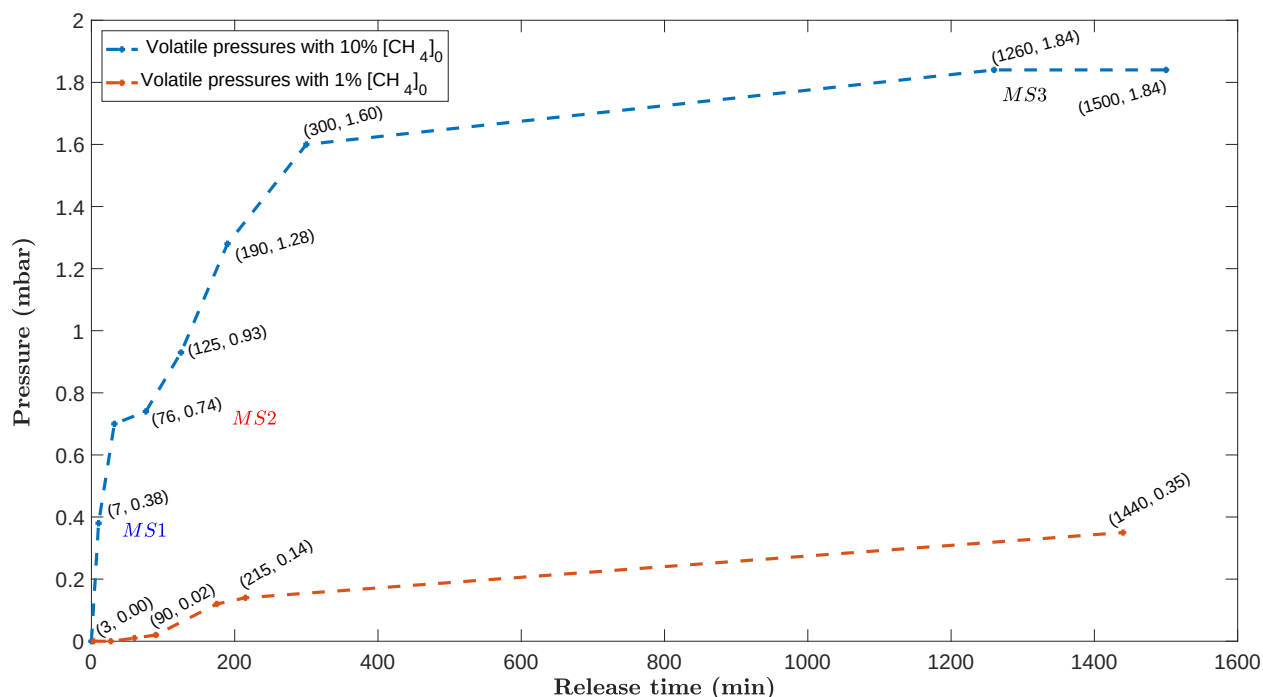
Fig. 3. (Top) Pressure evolution of the gas products according to degassing time in a 90-10% (blue) and 99-1% N_2-

CH_4 (red) gas mixture. Labeled at each data point are the times and vessel pressures, respectively. The *MS1* (-

130ºC, 0.38 mbar), *MS2* (-79ºC, 0.74 mbar), *MS3* (+22ºC, 1.84 mbar) color-coded labels correspond to the three

spectra of Fig. 4 taken at their corresponding temperatures and pressures, underlying significant detections at 10%

methane. (Bottom) Temperature evolution during degassing of the volatiles with the same color code for both mixing

ratios.

365

366   *3.1.1. Products released at temperatures below -100°C in the case of* [CH$_4$]$_0$ = 10%,

367

368   We are first interested in the molecules released below -100°C in the case of [CH$_4$]$_0$ = 10%,

369   which are not produced (or at least not in detectable quantities) in [CH$_4$]$_0$ = 1%.

370   As a first qualitative guess, we use the Antoine Law (Mahjoub et al., 2014) Eq. (1) to calculate

371   the vapor pressure of C$_2$H$_6$, which, at -180°C, is slightly above the triple point of -183.15°C (Fray

372   and Schmitt, 2009). C$_2$H$_6$ is indeed one of four volatiles expected to be present our final gas

373   mixture (Gautier et al., 2011), along with C$_2$H$_2$, C$_2$H$_4$, and HCN. We use the A, B, C parameters

374   from the NIST database (Carruth and Kobayashi, 1973). The low temperature used in the

375   present study is at the edge of the validity range for C$_2$H$_6$. Nonetheless, we extend this law's

376   validity domain and assume it to be applicable to these low-temperature conditions and thus

377   must consider this calculation as a first approximation only. The vapor pressure is calculated at -

378   180°C.

$$\log_{10}(P_s) = A - \left(\frac{B}{T+C}\right) \qquad (1)$$

379

380   For C$_2$H$_6$, we find P$_s$ = 5.7 x 10^2 mbar. This vapor pressure combined with the fact that we are

381   slightly above the triple point of C$_2$H$_6$ near the liquid/vapor equilibrium, shows that this species

382   will hardly condense.

383   HCN, C$_2$H$_2$ and C$_2$H$_4$ all have their triple points (Fray and Schmitt, 2009) at temperatures higher

384   than -180°C. They are listed in Table 1. Fray and Schmitt, 2009 provided a review of vapor

385   pressure relations obtained empirically and theoretically for a wide variety of astrophysical ices.

386   They fitted polynomial expressions to extrapolate the sublimation pressures and used

387   theoretical and empirical interpolation relations to obtain the coefficients of the polynomials. The

388   polynomial expression from Fray and Schmitt, 2009 is given Equ. 2. The polynomials (Table 1)

389   are noted A_i and T_p are the corresponding temperatures, -180°C (93K) in our case. The

390   sublimation pressures (P$_{sub}$) are presented in Table 1.

391

392

393    $$\ln(P_{sub}) = A_0 + \sum_{i=1}^{n} \frac{A_i}{T_i} \qquad (2)$$

394

395

396

	T_p (°C)	A_0	A_1	A_2	A_3	A_4	P_{Sub} (-180°C) in mbar
HCN	-14.15	1.39×10^1	-3.62×10^3	-1.33×10^5	6.31×10^6	-1.13×10^8	1.69×10^{-12}
C_2H_2	-81.15	1.34×10^1	-2.54×10^3	0	0	0	9.48×10^{-4}
C_2H_4	-169.15	1.54×10^1	-2.21×10^3	-1.22×10^4	2.84×10^5	-2.20×10^6	1.3×10^3

Table 1. Vapor pressures P_{sub} (mbar) calculated at 93K (-180°C) for HCN, C_2H_2 and C_2H_4. The T_p and A_i columns correspond to the triple points and coefficients of the polynomials of extrapolations, respectively, as given by Fray and Schmitt, 2009.

The larger values (Table 1) for the two C_2 hydrocarbons in comparison with HCN agree with a first substantial release of the light C_2 hydrocarbons at temperatures below -100°C. HCN contributes to the gas composition mainly in the second stage, for temperatures larger than -80°C, because of its low vapor pressure at colder temperatures.

The absence of C_2 hydrocarbons in the case of $[CH_4]_0$ = 1% is in agreement with the *ex-situ* analysis made in Gautier et al., (2011).

3.1.2. Detections by mass spectrometry

To go further in the analysis of the gas release, we monitored the gas phase composition by mass spectrometry at three threshold moments *MS1*, *MS2*, *MS3* for 10% methane and only in the final gas mixture for 1%.

In the case of 10% methane (Fig. 3 dashed blue line), the assigned *MS1*, *MS2* and *MS3* spectra are defined as the T, P conditions of -130°C and 0.38 mbar, -79°C and 0.74 mbar and +22°C and 1.84 mbar of products formed, respectively. *MS1* is representative of the first release stage occurring at temperatures lower than -100°C, *MS2* is on the pressure plateau beginning at -100°C, and *MS3* corresponds to the final gas mixture obtained. For 1% methane conditions, we will only focus on the last point, where a substantial volatile pressure was measured.

A first iteration at $[CH_4]_0$ = 10% was done. Mass spectra of the volatiles are shown Fig. 4. at different stages in their release after the plasma discharge, namely *MS1*, *MS2* and *MS3*.

425   -   *MS1*: 7min after stopping the cryogenic trap (blue line), C_1, C_2 and C_3 block species
426   have started to appear, with C_1 and C_2 (light volatiles of m/z < 30 amu) dominating
427   the spectrum. Masses 15 and 28 stand out for the C_1 and C_2 blocks, respectively.
428   Mass 28 cannot be attributed to N_2 as it was not trapped at -180°C during the
429   experiment. It can be attributed to ethylene C_2H_4 or ethane C_2H_6 as both molecules
430   are expected to be released at temperatures lower than -100°C and both have their
431   major fragment at m/z 28 according to the NIST database. However, the previous
432   ethane vapor pressure calculations and its triple point (Fray and Schmitt, 2009) show
433   that it could not condense. In these plasma conditions, it is risky to attribute m/z 29 to
434   methanimine (CH_2=NH) as the contribution of propane (C_3H_8) becomes non
435   negligible (Carrasco et al., 2012). m/z 29 corresponds indeed to the main peak in the
436   fragmentation pattern of C_3H_8. A few heavier volatiles in the C_3 and C_4 block are also
437   beginning to be detected. At m/z 44 we could also suspect the contribution of CO_2. A
438   blank mass spectrum of the mass spectrometer only has previously been measured
439   (Carrasco et al., 2012), showing the same intensity of 2 x 10^{-12} A at m/z 44 as the
440   one seen in Fig. 4 (blue plot), at low temperature. It corresponds to the weak air
441   signature within the mass spectrometer at a vacuum limit of about 3 x 10^{-8} mbar.
442   Consequently, the contribution of CO_2 observed in the mass spectra of Fig. 4 at m/z
443   44 is minor inside the chamber among the released products and corresponds to the
444   residual air in the mass spectrometer itself.

445

446   -   *MS2*: The main differences compared to *MS1* revolve around the C_3 and C_4 blocks
447   with the appearance of heavier hydrocarbons (red line, m/z > 50). Within the C_3
448   block, an important contribution appears at m/z 39, consistent with the cyclopropene
449   isomer C_3H_4. A significant increase is also observed at m/z 40 and 44 compatible
450   with the fragmentation pattern of propane C_3H_8 in the NIST database. No species
451   with masses higher than m/z 58 are detected yet.

452

453   -   *MS3*: Remarkable changes occur at this final stage (black line), where many new
454   species stand out. In the C_1 block, m/z 17 (NH_3) strongly increases to become the
455   dominating C_1 compound.
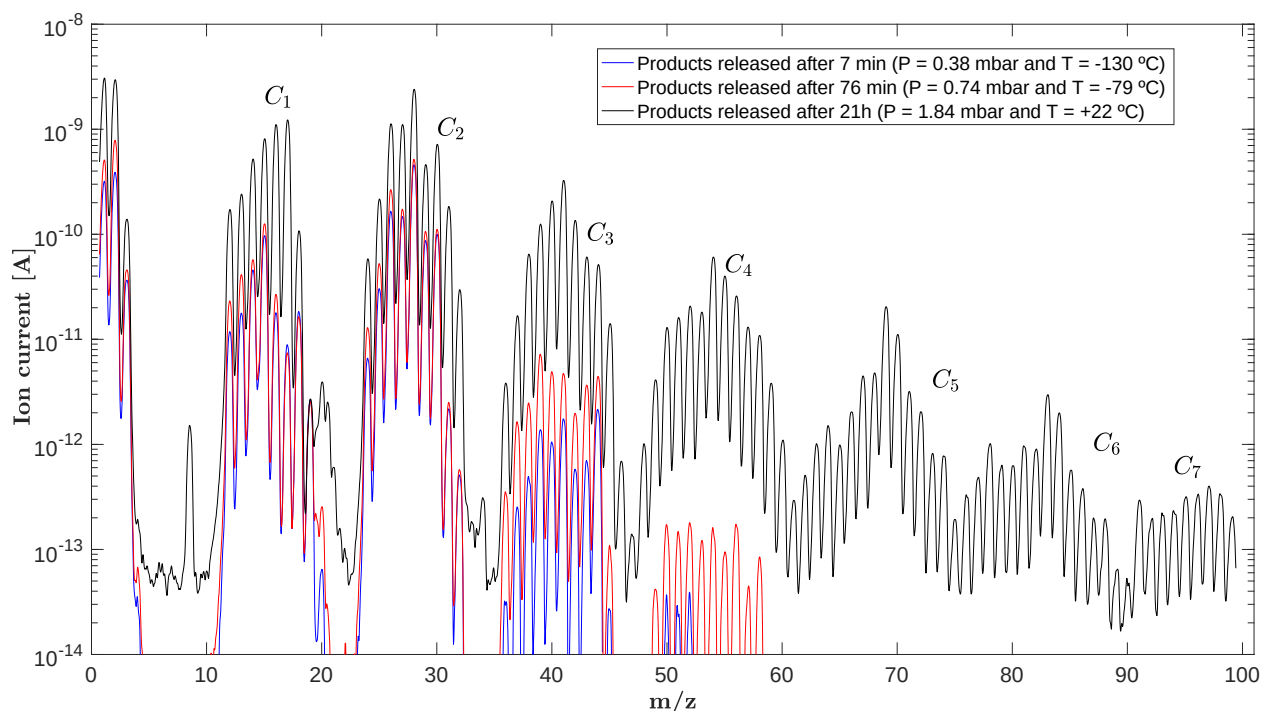
Fig. 4. Detection and evolution of several C_n blocks for $[CH_4]_0$ = 10%. Plots marked in blue, red and black represent intermittent spectra taken 7 min, 76 min and 21h after commencing volatile release back to room temperature (*MS1*, *MS2* and *MS3*, respectively). The indicated temperatures correspond to those taken at the start of a mass scan. Note that during a scan acquisition (~200s long), the temperature may change over 0.3 ºC to 23 ºC depending on the heating rates. The color code used here is the same as *MS1*, *MS2* and *MS3* of Fig. 3.

If we now compare the final stages obtained in the case of $[CH_4]_0$ = 1% and 10% on Fig. 3, the total pressure of volatiles obtained (0.35 mbar, blue line) is much less than in the case of $[CH_4]_0$ = 10% (red). Fig. 5 shows a comparison of the final states at $[CH_4]_0$ = 1% (brown) and $[CH_4]_0$ = 10% (blue), with the initial state (black), taken just before the volatile release at low-controlled temperature T = -180ºC. As expected from the lower final pressure, the mass spectrum is much less intense in the case of $[CH_4]_0$ = 1% than 10%. No signature is detected beyond the C_5 block for 1% whereas large intensities are found until the C_7 block in the case of 10%. However, the major peaks are the same in both cases. The C_1 block is dominated by m/z 17, accountable for ammonia. This important production, discussed in section 4.2, is a new result compared to the work by Gautier et al. (2011) and Carrasco et al. (2012). Indeed, as detailed in Carrasco et al. (2012), ammonia was hardly detectable with the analytical methods used in the two latter studies. The C_2 block has high peak intensities at m/z 26, 27, 28, 30 for $[CH_4]_0$ = 10% but the one at 28 stands out in both methane conditions, compatible with C_2H_4 or C_2H_6. The C_3 block is

477   dominated by m/z 41, accountable for acetonitrile CH_3CN; m/z 54 dominates C_4, which could

478   correspond to butadiene C_4H_6 or $C_2N_2H_2$ (HCN dimer). For $[CH_4]_0$ = 10%, the C_5, C_6 and C_7

479   blocks are dominated by masses 69, 83 and 97, respectively. The odd masses predominantly

480   detected suggest a strong contribution of N-bearing molecules in both conditions.

481   The intensity evolution of m/z 17, 26, 27, 28 and 41 over time are shown Figure 11 in the

482   Supplementary Material.

483

484
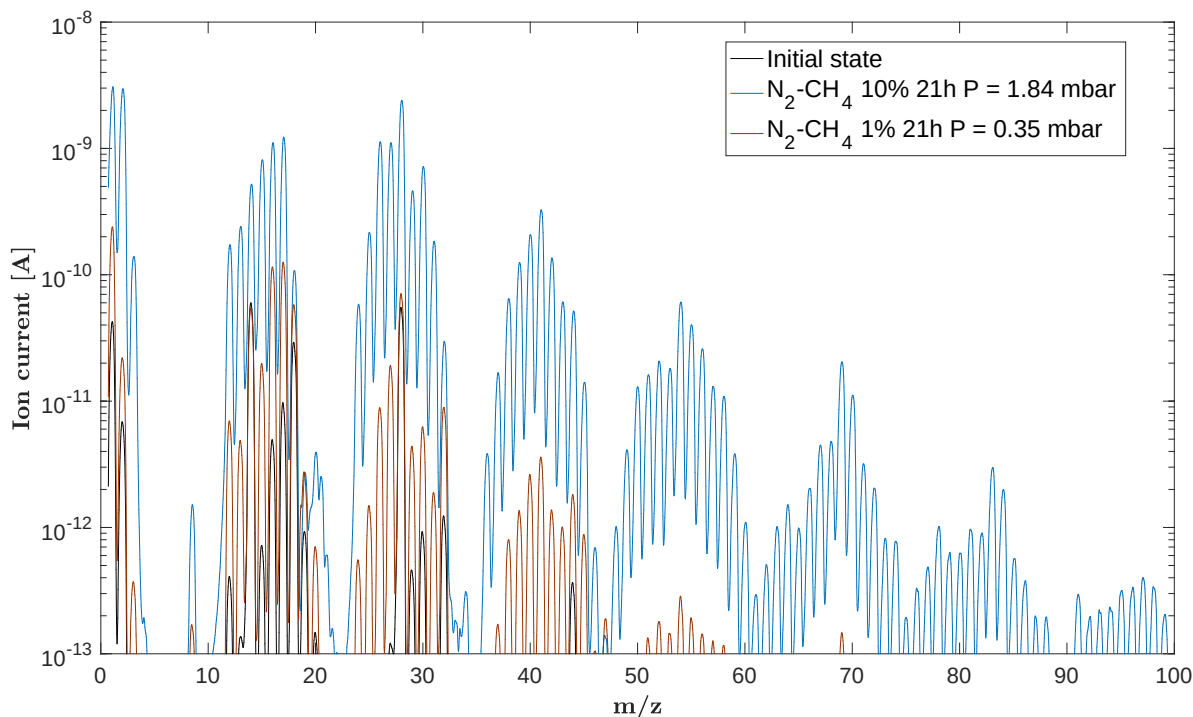
485   **Fig. 5.** Three superimposed spectra at different $[CH_4]_0$ concentrations. In black, the initial mass spectrum taken

486   before release of the volatiles, still at low-controlled temperature (and representative of the blank of our mass

487   spectrometer). In blue and brown, the final state of volatiles at $[CH_4]_0$ = 10% after 21h and $[CH_4]_0$ = 1% after 21h of

488   release, respectively.

489

490

491   *3.2 Monitoring and quantification using Mid-Infrared spectroscopy*

492

493   Alongside the neutral mass analysis, infrared spectra are simultaneously taken throughout the

494   release of the volatiles inside the chamber to provide quantification of these volatiles.

495   The measurement range is 650 cm^{-1} to 4000 cm^{-1} (2.5 µm to 15.4 µm) at a resolution of 1 cm^{-1}

496   during the release of the gas phase products analyzed *in situ*. Fig. 6 shows the spectra taken in

497　both initial methane conditions. The top plot was taken for a $[CH_4]_0$ = 10%, the bottom at $[CH_4]_0$

498　= 1%.

499　There is a clear discrepancy in the volatile products formed between the two conditions. $[CH_4]_0$

500　= 10% produces $–CH$ and $–CH_2$ compounds visible in the stretching mode region 3,000-3,500

501　cm^{-1} that are absent in the $[CH_4]_0$ = 1% case. Likewise, there is a relatively far greater

502　absorption of molecules bearing C=N and C=C bonds (~1,500 cm^{-1}) with $[CH_4]_0$ = 10%. Fig. 6

503　(bottom) also has a large, broad absorption spread out over 2,000-2,500 cm^{-1} absent in the top

504　figure. These signatures could correspond to a scattering feature of solid grains in suspension

505　which could be the result of the released precursors reacting post-discharge. Furthermore, in

506　Sciamma-O'Brien et al. (2010), it had been shown that the gas to solid conversion yield was

507　more important in the case of the 1% experiment than in the 10% experiment, in agreement with

508　a higher amount of N-bearing gas phase products compared to hydrocarbons in the 1%

509　experiment. The present results are consistent with this previous study.

510

511

512

513
514
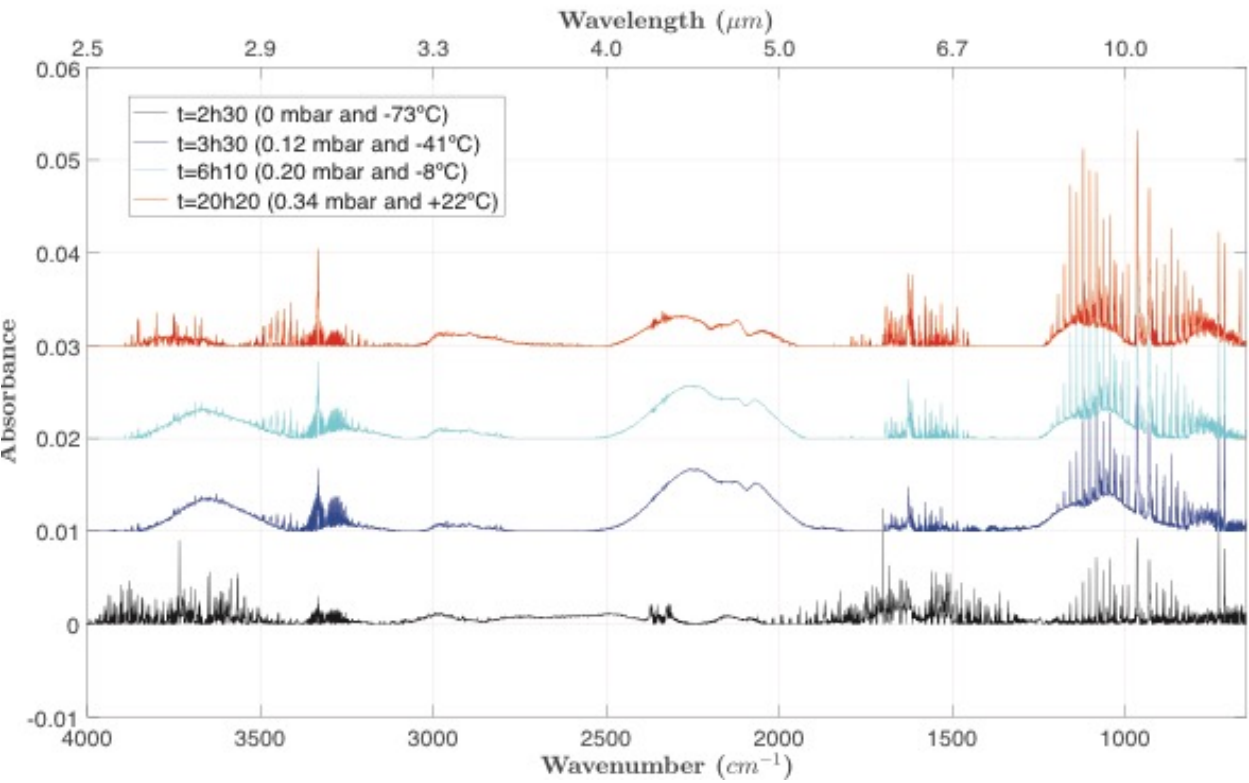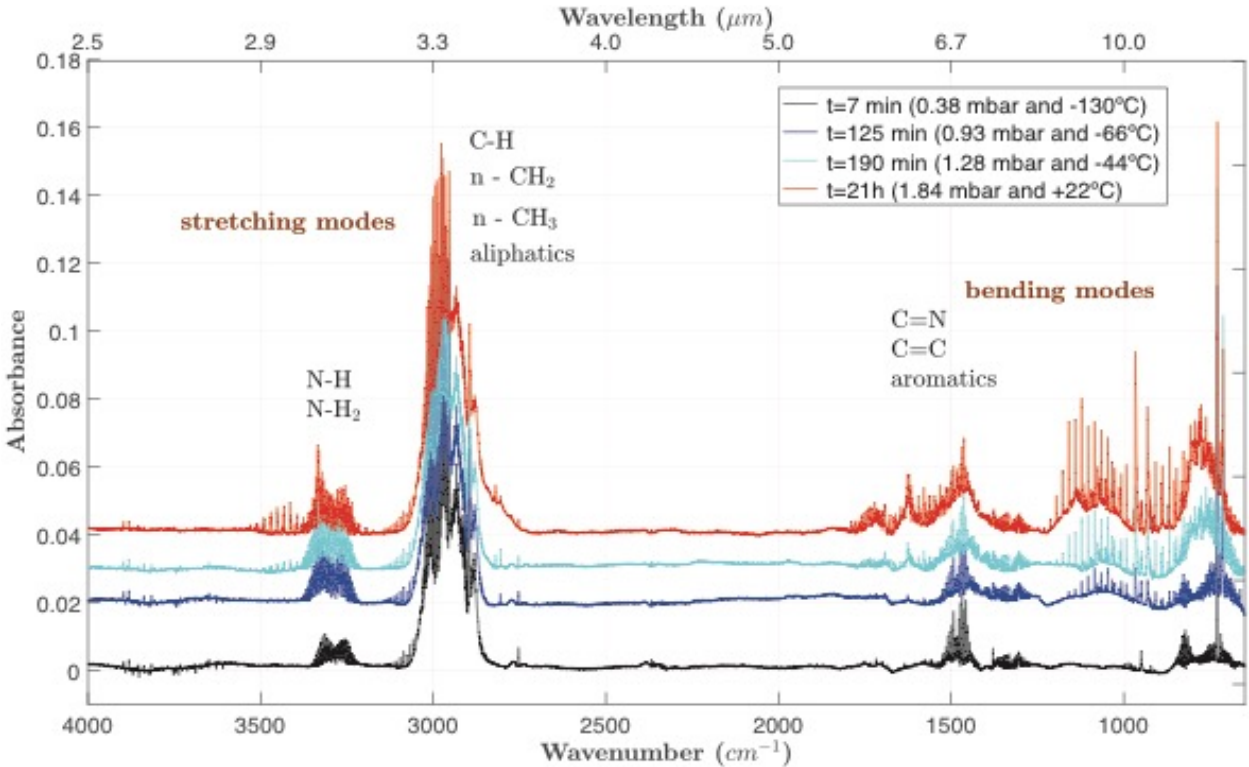
515   **Fig. 6** FT-IR spectra of the volatiles taken after the 90-10% (top) and 99-1% (bottom) N_2-CH_4 plasma conditions,
516   plotted with an arbitrary absorbance against a 650-4000 cm^{-1} wavenumber range. The volatile density produced
517   during the plasma discharge is being incrementally released and analyzed through IR spectroscopy. Top: Total gas
518   pressures of 0.38 mbar (-130ºC), 0.93 mbar (-66ºC), 1.28 mbar (-44ºC) and 1.84 mbar (+22ºC) are shown in black,
519   blue, cyan and red, respectively. Bottom: Total measured gas pressures of 0 mbar (-73ºC), 0.12 mbar (-41ºC), 0.20
520   mbar (-8ºC) and 0.34 mbar (+22ºC) with the same color code. One clear difference is in the absence of any
521   substantial aliphatic compounds (2800-3100 cm^{-1}) at $[CH_4]_0$ = 1% (bottom) that stand out at $[CH_4]_0$ = 10% (top).

524   Among all the signatures observed, we identified and calculated the concentrations of four
525   volatiles as they are released in the chamber: NH_3, C_2H_2, C_2H_4, and HCN. These species are
526   listed in Table 2. Ammonia (NH_3), acetylene (C_2H_2), hydrogen cyanide (HCN), ethylene (C_2H_4),
527   are all species present at ionospheric and/or stratospheric altitudes on Titan, considered to be
528   key in the formation of Titan's aerosols (Hanel et al., 1981; Kunde et al., 1981; Maguire et al.,
529   1981; Wilson and Atreya, 2003, 2004) and formed in the upper atmosphere (Hörst, 2017).

Selected species	$C_xH_yN_z$	Main absorption bands (cm^{-1})	Detected in Titan's atmosphere
Ammonia	NH_3	962 (10.4 µm)	1, 4 (upper limit inferred)
Acetylene	C_2H_2	729.25 (13.7 µm)	1, 2, 6
Hydrogen cyanide	HCN	712.3 (14.0 µm)	1, 5, 6, 7, 8
Ethylene	C_2H_4	949.3 (10.5 µm)	1, 3

536   **Table 2.** Four major volatile compounds detected and analyzed by infrared spectroscopy at $[CH_4]_0$ = 1% and $[CH_4]_0$ =
537   10%. The main infrared absorption bands which were used for density calculations are also given. References
538   are 1: Vinatier et al. (2007), 2: Cui et al. (2009), 3: Coustenis et al. (2007), 4: Nelson et al. (2009), 5: Paubert et
539   al. (1984), 6: Teanby et al. (2007), 7: Moreno et al. (2015), 8: Molter et al. (2016). For more details on the
540   bands and absorption cross-sections used for the molecular density calculations, the reader is referred to Table
541   3 and Figures 9 and 10 of the Supplementary Material.

542

543 To track the production and evolution with time/temperature of these four compounds, we used

544 *in situ* infrared quantification. By using Beer-Lambert's Law (Eq. 3), we can calculate the

545 concentration of any given gas phase product.

546

$$I_t = I_0 \times e^{-l.\sigma.N} \tag{3}$$

547

548 I_t, I_0 and l are, respectively, the transmitted, incident intensities, optical path (cm) and σ the

549 absorption cross-section (cm^2.molecule^{-1}) given by the Pacific Northwest National Lab (PNNL),

550 University of Washington (Sharpe et al., 2004), GEISA (Armante et al., 2016) and ExoMol

551 (Harris et al., 2006; Hill et al., 2013; Tennyson et al., 2016) databases. In addition, *N* is the

552 molecular density (cm^{-3}). The absorption *A* is as follows:

553

$$A_{(\lambda)} = l \times \sigma_{(\lambda)} \times N \tag{4}$$

554

555 Using the integrated experimental absorption *A* with the integrated database absorption

556 cross-section σ between the two wavelengths λ_1 and λ_2, (4) becomes:

$$\int_{\lambda_1}^{\lambda_2} A d\lambda = l \times N \times \int_{\lambda_1}^{\lambda_2} \sigma d\lambda \tag{5}$$

557 So, we obtain the molecular number density *N* (molecules.cm^{-3}):

558

$$N = \frac{1}{l} \times \frac{\int_{\lambda_1}^{\lambda_2} A d\lambda}{\int_{\lambda_1}^{\lambda_2} \sigma d\lambda} \tag{6}$$

559

560 Number densities are derived over a wavenumber range (see Table 3 of the Supplementary

561 Material), covering the absorption band considered for each species.

562

563 The main absorption band of each species was taken for all cases. The density results for both

564 conditions are shown Fig. 7 and Fig. 8. For the detailed number density calculation results and

565 data points used with the specific integration bands, the reader is invited to peruse the

566 Supplementary Material of the online version of this article.

567 The 962 cm^{-1} (10.4 μm) NH_3 assigned band refers to the υ_2 N-H symmetric deformation. It is

568 part of the NH_3 doublet at 930 and 960 cm^{-1}, caused by the motion of nitrogen through the plane

569 of the three protons leading to an energy barrier. In the case of C_2H_2, we used acetylene's

570 729.25 cm^{-1} frequency of oscillation (13.7 μm). This band corresponds to the symmetric CH

571 bending mode υ_5 of every other C and H atom to its respective neighboring atom. For HCN, we

572 used the fundamental υ_2 bend frequency at 712 cm^{-1} (14.0 μm); C_2H_4 the υ_7 CH_2 wag

573 deformation at 949 cm^{-1} (10.5 μm). C_2H_4 centered at 950 cm^{-1} is surrounded by the NH_3 doublet

574 at 930 and 960 cm^{-1}. This absorption represents the fundamental absorption of ammonia's υ_2

575 normal vibrational mode. The motion of nitrogen through the plane of the three protons causes

576 this vibration with an energy barrier. For a summary on each band and frequency used, the

577 reader is referred to Table 3 of the Supplementary Material.

578

579 Molecular number densities at N_2/CH_4 : 99/1% are listed in Table T-4. The measurements taken

580 at t_{1-6} correspond approximately to 30 min, 60 min, 120 min, 180 min, 1200 min and 1440 min,

581 respectively. Three datasets were acquired after three experiments in the same initial

582 conditions. At this point, it is noteworthy to remember that t_0 represents the time when the

583 plasma conditions and cryo-trap cooling are ended (Fig. 3), and thus when the condensed

584 volatiles can effectively desorb from the chamber still under vacuum walls into the gas phase.

585 Overall, ammonia is the most dominant C_1 neutral (~ 1.1 x 10^{15} cm^{-3}) produced at 1% CH_4,

586 confirming its high intensity at m/z 17 detected in mass spectrometry (Fig. 4). C_2H_2 and C_2H_4

587 also reached relatively high abundance ~ 3.2 x 10^{12} cm^{-3} and ~ 9.9 x 10^{12} cm^{-3}, respectively.

588 These number densities correspond to the final measurements.

589
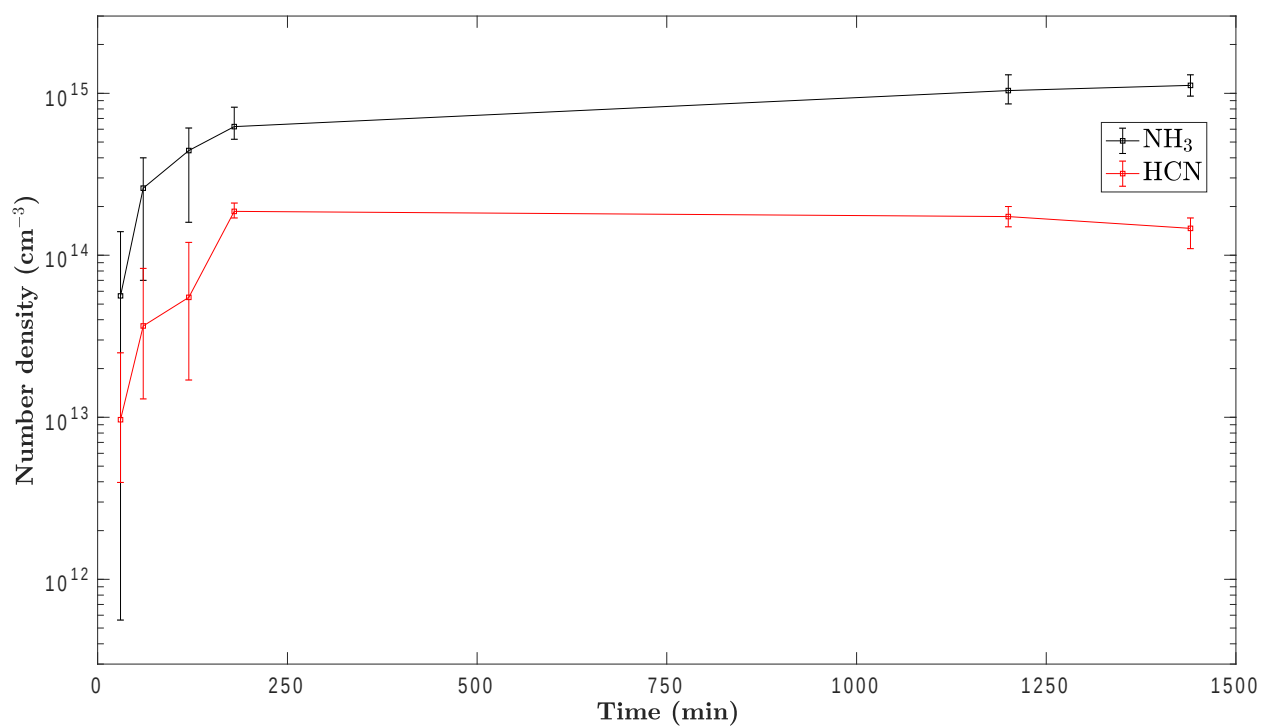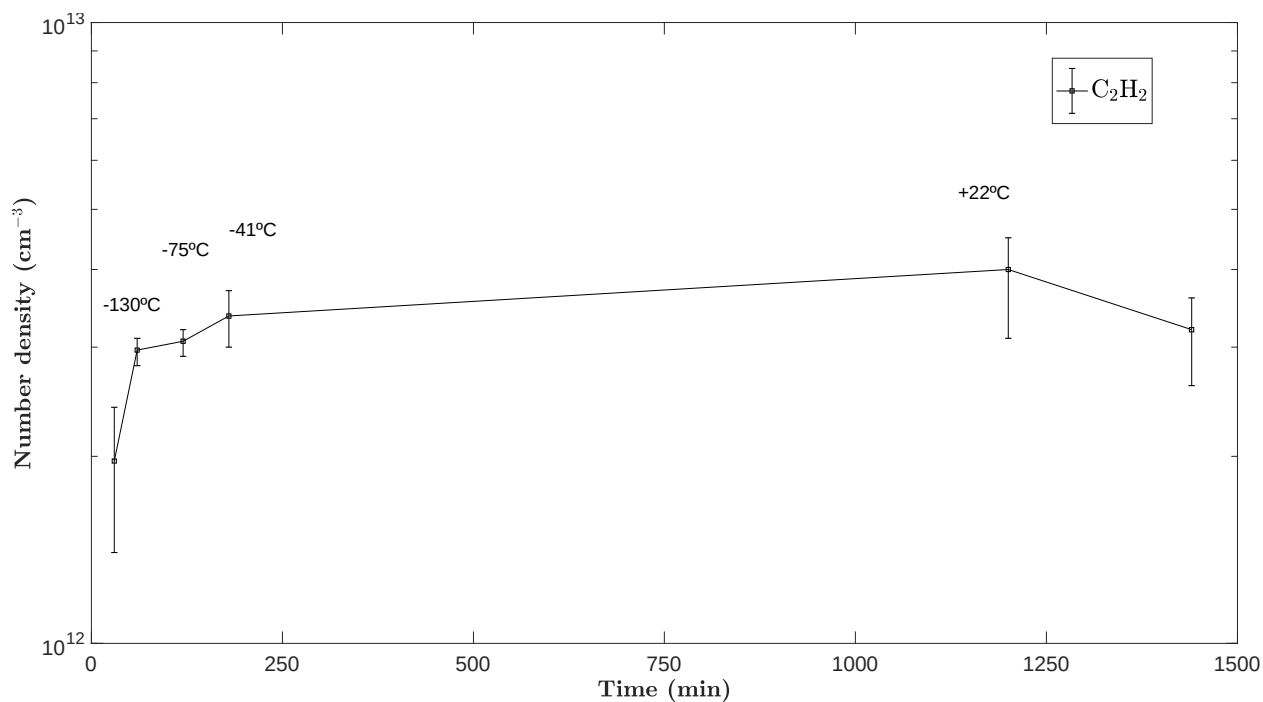
590
591
592   **Fig. 7.** 1% methane conditions. Top: Molecular densities and average fitted kinetic profiles of C_2H_2 and C_2H_4. Bottom:
593   NH_3 and HCN. Approximate temperatures are also labeled over each data point. The error bars represent the
594   dispersion of the data points for all three experiments (Table 4 and 5 of the online version of this article).

26

595   Fig. 8 shows the same kinetic profiles from a 10% methane initial gas mixture, with the
596   molecular densities listed in Table T-4. The C_2 species all reach concentrations at an order of
597   magnitude higher than those at 1%, correlating with the higher methane concentration initially
598   injected, which promotes the production of hydrocarbon species. C_2 species are thus strongly
599   favorably produced with increasing methane concentrations. This is especially notable with the
600   amount of HCN produced ($\sim 1.2 \times 10^{15}$ cm^{-3}) in the 10% $[CH_4]_0$ condition.
601

602
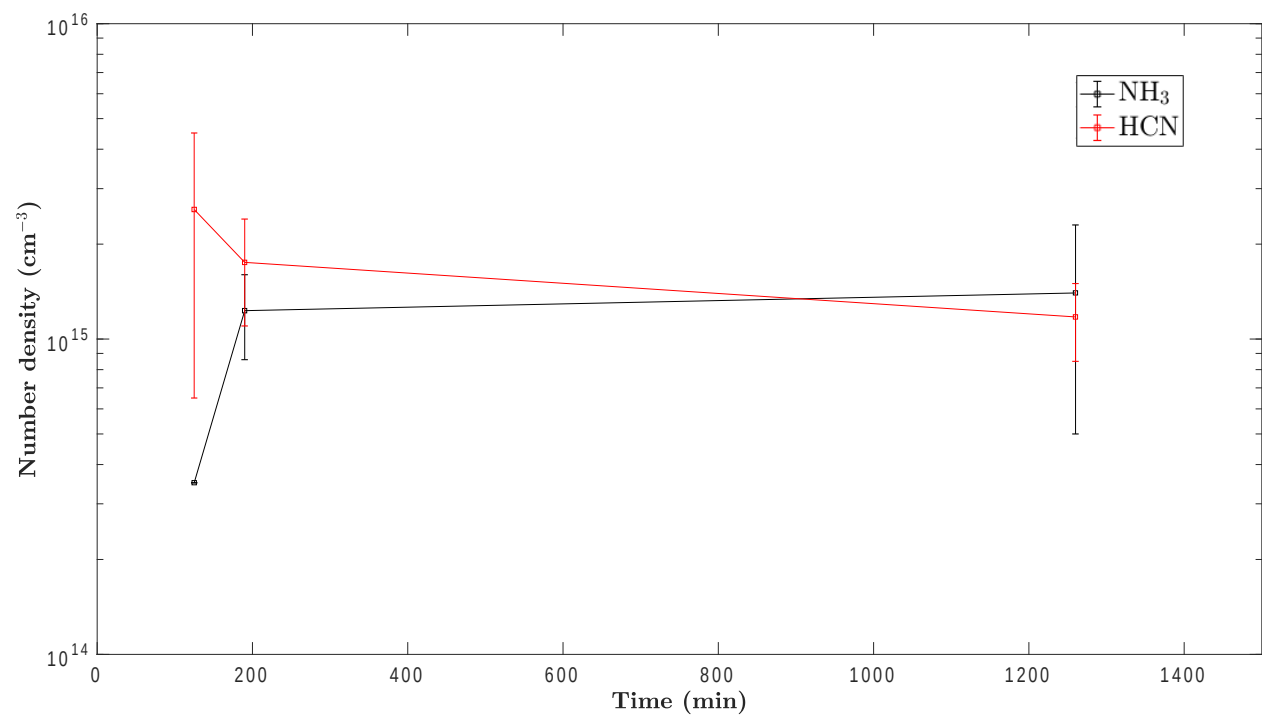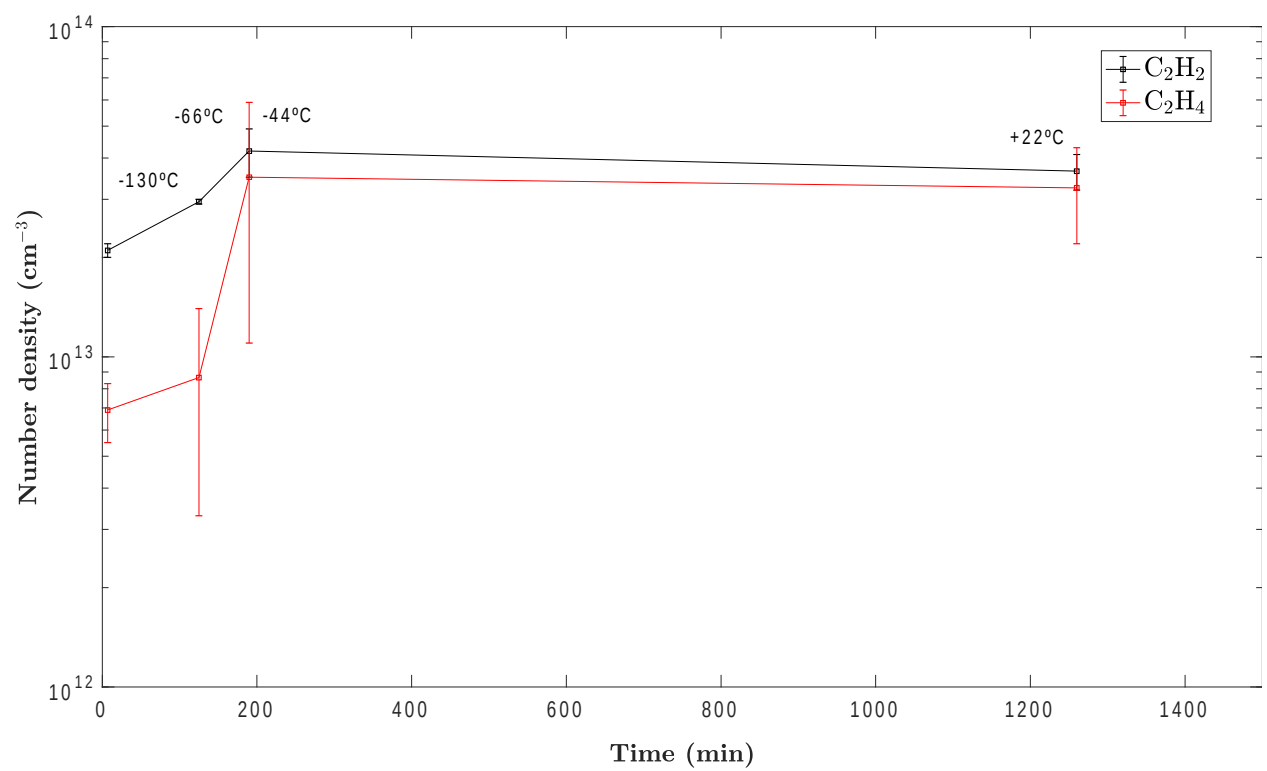
603
604 **Fig. 8.** 10% methane conditions. Top: Molecular densities and average fitted kinetic profiles of C_2H_2 and C_2H_4.
605 Bottom: NH_3 and HCN. Approximate temperatures are also labeled over each data point. The error bars represent
606 the dispersion of the data points for both experiments (Table 4 and 5 of the online version of this article).

607

608

609   ***3.3 Methane consumption and hydrocarbon yield***

610

611   With a 10% CH_4 mixing ratio, the condition with the most products, we consider the CH_4

612   consumption to provide yield estimates on the carbon conversion to hydrocarbon gas products.

613   We note D as the total gas flow rate (N_2-CH_4) into the chamber in standard conditions. We first

614   calculate the amount of CH_4 consumed in standard conditions (mg.h^{-1}), with D = 55 sccm. If n_{tot}

615   is the total number of gas phase moles entering the reactor per second, the ideal gas law

616   becomes:

617

$$\frac{d_{ntot}}{dt} = \frac{P_0}{R \times T_0} \times D \qquad (7)$$

618

619   With P_0 the gas pressure in *Pa*, *R* the ideal gas constant, *T* the absolute temperature (300 K),

620    $d_{ntot}/dt = 2.22 \times 10^{19}$ molecules.s^{-1}. As seen previously, with a mixing ratio of $[CH_4]_0$ = 10%, we

621   find a CH_4 consumption of 52%. So,

622

$$\frac{dn_{CH_{4cons}}}{dt} = D_{CH_4} \times CH_{4cons} \times d_{ntot}/dt \qquad (8)$$

623

624   And the methane consumption rate is $dn_{CH_{4cons}}/dt = 1.15 \times 10^{18}$ molecules.s^{-1}. As the plasma

625   runs for 2h, the total methane consumption is $n_{CH_{4cons}}(2h)/dt = 8.28 \times 10^{21}$ molecules. The

626   total volume of the PAMPRE reactor is ~ 28$\times$10^3 cm^3. Consequently, there is a CH_4 total

627   consumption of about 2.9×10^{17} molecules.cm^{-3} over the 2h of the plasma discharge. With a

628   calculated HCN total number of molecules of ~ 1.2 x 10^{15} cm^{-3}, HCN accounts for ~ 0.4% of the

629   carbon conversion from the consumed CH_4, while it is ~ 0.3 ‰ and 0.2 ‰ for C_2H_2 and C_2H_4,

630   respectively.

631

29

632   **IV) Discussion**

633

634   *4.1 Volatile discrepancies at $[CH_4]_0$ = 1% and $[CH_4]_0$ = 10%*

635

636   There are evident differences in the volatile products formed in both methane concentrations
637   used in this study (Fig. 3, Fig. 6, Tables T-3 and T-4 of the online version of this article). Despite
638   obtaining ~ 1.84 mbar solely in volatile products with 10% methane and ~ 0.35 mbar at 1%
639   methane, both spectra on Fig. 5 appear to qualitatively show the same nitrogen-bearing odd
640   mass compounds, albeit at different intensities. One major discrepancy though, lies in the
641   overwhelming amount of hydrocarbon species produced at 10% methane. The C_2 block is
642   dominated by the m/z 28 amu signal (Fig. 5), dominating the rest of the spectra, which
643   according to the NIST database, corresponds to ethylene and ethane's main fragment (this
644   mass cannot be linked to a release of N_2, as the cryotrap temperatures were not cold enough to
645   trap any nitrogen during the experiment). However, the vapor pressure indicates that ethane is
646   difficult to trap, and so m/z 28 can be mainly attributed to C_2H_4. Furthermore, the I_{30}/I_{28} ratio of
647   the absolute intensities in the mass spectra at m/z 30 and m/z 28 amu correspond to the ones
648   given by NIST, ~ 30-35%. On Titan, short-lived species such as C_2H_4 remain tantalizing to
649   study, as they experience stratospheric dynamical processes with changing mixing ratios. By
650   preventing the condensation of N_2, this study shows how m/z 28 may be attributed to C_2H_4 as
651   one of the most abundant hydrocarbons at 10% CH_4.

652

653

654   *4.2 Ammonia*

655

656   Moreover, NH_3 stands out as being the most dominant N-bearing molecule in both $[CH_4]_0$ =
657   1% and $[CH_4]_0$ = 10% conditions, with final calculated concentrations of ~ 1.1 x 10^{15} and ~ 1.4 x
658   10^{15} molecules.cm^{-3}, respectively.
659   Ammonia production was previously shown to be positively correlated with an increasing
660   methane concentration (Carrasco et al., 2012). However, the latter study did not consider
661   ammonia detection due to lack of a quantification approach as well as the m/z 17 H_2O fragment
662   contamination. NH_3, as well as HCN, are nitrogen-bearing volatiles of utmost importance related
663   to prebiotic chemistry in reducing atmospheric environments. So, studying NH_3 in Titan's upper
664   atmosphere is crucial to understanding the chemical pathways leading to the formation of
665   aerosols and how it is incorporated in them. Cassini/INMS analyses of early Titan flybys (Vuitton

666   et al., 2007) first reported the presence of ammonia in the ionosphere, which was later more
667   robustly confirmed by Cui et al. (2009). Yelle et al. (2010), Carrasco et al. (2012), Loison et al.
668   (2015) discussed NH_3 chemical pathways. As such, the formation of ammonia in Titan's
669   atmosphere is still unclear, though it is thought to most likely involve methanimine CH_2NH which
670   itself acts as an important source for NH_2 radicals in plasma conditions, to eventually forming
671   NH_3. An ionic characterization of pathways and reactions pertaining to ammonia production is
672   out of the scope of this paper.
673   Yelle et al. (2010) proposed an explanation for the production of NH_3. Indeed, NH_3 is being
674   photochemically formed in the upper atmosphere and fed down into the stratosphere. While
675   photochemical models (Lara et al., 1996; Krasnopolsky, 2009) did not initially predict the
676   formation of NH_3 in the upper atmosphere, its production can be explained through ion reactions
677   (Yelle et al., 2010), by measuring the protonated ion NH_4^+. Based on the long chain reaction
678   forming NH_3 detailed by Yelle et al. (2010) and its importance in our experimental results (major
679   nitrogen-bearing molecule), the contribution of nitrogen-bearing functional groups (e.g. amines,
680   nitriles or imine) or their contribution to eventually be incorporated into the organic aerosols
681   seems pertinent. This appears to be the case for NH_3, being the main N-bearing compound. In
682   more advanced environments whether on Titan (Neish et al., 2009) or in the interstellar medium
683   (e.g. Largo et al., 2010), NH_3 remains an open and current topic to study prebiotic chemistry.
684
685   *4.3 C_2H_4 pathways to tholin formation*
686
687   The presence of ethylene in the ionosphere (Waite et al., 2007) and stratosphere (e.g.
688   Coustenis et al., 2007) is well established. However, similar to the other volatiles chosen in this
689   study, its influence and participation in tholin formation needs to be further investigated. The
690   relative concentration of C_2H_4 in Titan's atmospheric column is subject to distinct features. It
691   was first noted by Coustenis et al. (2007) and Vinatier et al. (2007) how the retrieved
692   stratospheric vertical abundances of C_2H_4 from Cassini/CIRS data showed both a unique
693   decrease in the mixing ratios towards high northern latitudes as well as being the only species
694   whose mixing ratio decreases with altitude at 15ºS near the equator. Compared to other C_2
695   molecules (e.g. C_2H_2, C_2H_6, HCN), C_2H_4 is unique in that its mixing ratio decreases with altitude
696   at equatorial and northern polar latitudes. One hypothesis given by Vinatier et al. (2007) was
697   that C_2H_4 (along with C_4H_2 and CH_3C_2H), is subject to a photodissociative sink along with
698   equatorward transport from the winter polar vortex in the lower stratosphere and troposphere

699 (Crespin et al., 2005), essentially removing it away from the gaseous atmosphere. This sink
700 could eventually be the multiple haze layer.

701

702 As discussed previously and shown Fig. 5 and Table 5 (Supplementary Material), C_2H_4 is an
703 important C_2 compound in the 10% $[CH_4]_0$ mixture. Similar experiments (Gautier et al., 2014)
704 argued that (although in the absence of a cooling plasma system) tholins are formed with CH_2
705 patterns, coherent with C_2H_4 putatively acting as a strong gaseous precursor. This study comes
706 in agreement, at least on a tholin formation scale that C_2H_4 participates in their formation. This
707 experimental result also confirms that, if the stratospheric multiple haze layer is indeed the sink
708 to this molecule (Vinatier et al., 2007), the latter can easily take chemical pathways leading to
709 the formation of aerosols.
710 Pathways involving C_2H_4 (alongside C_2H_2) loss have been suggested by Yelle et al. (2010).
711 They proposed that C_2H_4 (and C_2H_2) reacts with NH radicals (Reaction 9) to produce heavier
712 nitrile molecules such as CH_3CN (Reaction 10) or the cyanomethylene radical HC_2N.

713

$$N^+ + CH_4 \rightarrow CH_3^+ + NH \qquad (9)$$

714

$$NH + C_2H_4 \rightarrow CH_3CN + H_2 \qquad (10)$$
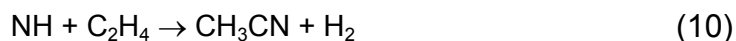
715   The formation of NH radicals, reaction (9), occurs in ion chemistry conditions through
716 proton exchange, while these same radicals can then react with ethylene, reaction (10) in
717 neutral conditions. Given the large abundance of produced NH_3, it is possible that NH radicals
718 were formed and reacted with C_2H_4 during our 2h plasma, which incidentally is favorably
719 produced with increasing CH_4 concentration (Reaction 9).
720 Interestingly, C_2H_4 is implicated in NH_3 formation. According to Yelle et al. (2010),

721

$$NH_2 + H_2CN \rightarrow NH_3 + HCN \qquad (11)$$

722 Prior to this, the formation of the amino radical NH_2 involves ion chemistry, with the following
723 ion-neutral reaction:

724

$$N^+ + C_2H_4 \rightarrow NH_2 + C_2H_2^+ \qquad (12)$$

725   Thus, C_2H_4 in our plasma may participate in the production of heavier nitrile species or
726   ammonia during the plasma discharge.

727

728

729   *4.4 HCN production*

730

731   Hydrogen cyanide in Titan's atmosphere is well documented and known to be the most
732   abundant nitrile trace volatile (e.g. Kim et al., 2005; Vinatier et al., 2007), with high mixing ratios
733   at stratospheric altitudes in the northern polar regions.

734   HCN is also of prime importance in the search for prebiotic conditions in the solar system
735   and beyond (Oró, 1961) as well as being one of the precursors to amino acids and peptides
736   (Oró, 1961; Hörst et al., 2012; He and Smith, 2014; Rahm et al., 2016). In addition, the
737   chemistry of HCN mainly relies on its relatively high polarity and quite strong $C{\equiv}N$ triple bond,
738   with a bond dissociation energy D(H-CN) of ~ 5.2 eV calculated by photodissociation and
739   photoionization models (Berkowitz, 1962; Davis and Okabe, 1968; Cicerone and Zellner, 1983).
740   Thus, making it a relatively stable molecule.

741   As shown Figs. 7 and 8, HCN is one of the most abundant products formed in both $[CH_4]_0$ = 1%
742   and $[CH_4]_0$ = 10% conditions, with ~ 1.5 x 10^{14} cm^{-3} and 1.2 x 10^{15} cm^{-3} on average,
743   respectively. Carbon yield calculations stresses the carbon conversion to HCN (~ 0.4%), while
744   other C_2 species all are favorably produced by an order of magnitude at 10% CH_4 than at 1%
745   CH_4.

746   HCN and HCN-based copolymers are also known to participate in the chemical growth
747   patterns of tholin formation (Pernot et al., 2010; Gautier et al., 2014) along with the CH_2
748   monomer, which is in agreement with the idea that haze forming acts as an HCN sink in the
749   stratosphere (McKay, 1996; Vinatier et al., 2007). This study seems to confirm the prevalent role
750   of HCN in the formation of tholins.

751

752

753

V) Conclusions

The present study was aimed at expanding previous work focused on the volatile production and their participation in tholin production using a cold dusty plasma experiment (Gautier et al., 2011; Carrasco et al., 2012), but with one major twofold novelty (i) the ability to trap these volatiles *in situ* within our plasma reactor with a new experimental setup at low-controlled temperatures, and (ii) quantitatively analyze their formation using IR spectroscopy. It is important to be cautious in interpreting these quantitative results, as three (T, P and t) parameters change simultaneously during the sublimation phase entailing possible unsuspected ice-volatile chemistry. The approach we took was solely focused on the gas phase. Indeed, these volatiles, still poorly understood and which give Titan its unique nature of being one of the most chemically complex bodies in the Solar System, act as substantial gas phase precursors to the formation of Titan's organic aerosols populating its haze layers. Hence, simulating ionosphere conditions is crucial in constraining the volatile population, its reactivity and potential chemical pathways.

Major discrepancies exist between the two initial methane concentrations we used, 1% and 10%, with many more hydrocarbons formed in the latter case (detection of C_7 species), but with similar amounts of N-bearing species, only at different concentrations. Our results confirm the important role of C_2 species in the tholin precursor volatile family (m/z 28 e.g.), as well as that of NH_3. One of them, ethylene C_2H_4, being a relatively major C_2 hydrocarbons, might even reveal an important "hub" role at least at 10% $[CH_4]_0$ through which specific chemical pathways involving C_2H_4 are favored (see Section 4.3). The importance of C_2H_4 might also be relevant at 1% $[CH_4]_0$ although this is difficult to assess in this study due to the cryotrapping efficiency which is not optimum at -180ºC to quantify it, as suggested by the thermodynamical calculations and mass spectra during the discharge. Eventually, tholins themselves may be benefitting from the incorporation of C_2H_4, which itself stresses the value of considering a yet unaccomplished fully-coupled ion and neutral chemistry study. This is out of the scope of this paper, as the cryo-trap system prevents the formation of tholins. These experiments have also shown a strong incorporation of carbon into HCN, along with NH_3 being a competitive product to HCN, especially with a $[CH_4]_0 = 1\%$ (an order of magnitude more in final concentration).

Future compelling work to expand this study might be to consider other molecular families participating in the neutral reactivity, therefore increasing our knowledge of volatile chemistry

788 precursor to tholin production. In addition, adding selected volatiles such as HCN, an important
789 nitrile, in trace amounts into our gaseous mixture would improve the understanding of its
790 influence on the chemical reactivity in plasma conditions in future work. Moreover, predicting ion
791 densities and characterizing ion-neutral reactions in these conditions would be key to
792 understanding their incorporation into the solid phase and validating chemical pathways which
793 are still largely unknown in Titan ionosphere simulations. Perhaps most importantly, a fully-
794 coupled ion-neutral characterization would fundamentally bring credence to understanding the
795 complex organic realm encompassing Titan's gas phase chemistry.
796
797
798
799
800
801
802
803
804
805
806
807
808
809
810
811
812
813
814
815
816
817
818
819

820

821

822

823 **Acknowledgements**

824

829

830

831

832

833

834

835

836

837

838

839

840

841

842

843

844

845

846

847

848

849

850

851

References

852 **References**

853

854 Achterberg, R.K., Gierasch, P.J., Conrath, B.J., Michael Flasar, F., Nixon, C.A., 2011. Temporal
855   variations of Titan's middle-atmospheric temperatures from 2004 to 2009 observed by
856   Cassini/CIRS. Icarus 211, 686–698. doi:10.1016/j.icarus.2010.08.009

857 Alcouffe, G., et al., 2010. Capacitively coupled plasma used to simulate Titan's atmospheric
858   chemistry. Plasma Sources Sci. Technol. 19, 15008. doi:10.1088/0963-0252/19/1/015008

859 Alves, L.L., Marques, L., Pintassilgo, C.D., Wattieaux, G., Es-sebbar, E., Berndt, J., Kovacević,
860   E., Carrasco, N., Boufendi, L., Cernogora, G., 2012. Capacitively coupled radio-frequency
861   discharges in nitrogen at low pressures. Plasma Sources Sci. Technol. 21, 45008.
862   doi:10.1088/0963-0252/21/4/045008

863 Armante, R., Scott, N.A., Ch, A., Cr, L., Bouhdaoui, A., Crevoisier, C., Capelle, V., Boonne, C.,
864   2016. The 2015 edition of the GEISA spectroscopic database. J. Mol. Spectrosc.

865 Atreya, S., Donahue, T., Kuhn, W., 1978. Evolution of a nitrogen atmosphere on Titan. Science
866   (80-.).

867 Berkowitz, J., 1962. Heat of formation of the CN radical. J. Chem. Phys. 1555, 2533–2539.
868   doi:10.1063/1.1732330

869 Bezard, B., Paubert, G., 1993. Detection of acetonitrile on Titan.

870 Blagojevic, V., Petrie, S., Bohme, D.K., 2003. Gas-phase syntheses for interstellar carboxylic
871   and amino acids. Mon. Not. R. Astron. Soc. 339. doi:10.1046/j.1365-8711.2003.06351.x

872 Brown, M.E., Bouchez, A.H., Griffith, C. a, 2002. Direct detection of variable tropospheric clouds
873   near Titan's south pole. Nature 420, 795–797. doi:10.1038/nature01302

874 Brown, R.H., Lebreton, J.P., Waite, J.H., 2009. Titan from Cassini-Huygens, Springer. ed.
875   Springer.

876 Cable, M.L., Hörst, S.M., Hodyss, R., Beauchamp, P.M., Smith, M.A., Willis, P.A., 2012. Titan
877   tholins: Simulating Titan organic chemistry in the Cassini-Huygens era. Chem. Rev. 112,
878   1882–1909. doi:10.1021/cr200221x

879 Carrasco, N., Alcaraz, C., Dutuit, O., Plessis, S., Thissen, R., Vuitton, V., Yelle, R., Pernot, P.,
880   2008. Sensitivity of a Titan ionospheric model to the ion-molecule reaction parameters.
881   Planet. Space Sci. 56, 1644–1657. doi:10.1016/j.pss.2008.04.007

882 Carrasco, N., Gautier, T., Es-sebbar, E. touhami, Pernot, P., Cernogora, G., 2012. Volatile
883   products controlling Titan's tholins production. Icarus 219, 230–240.
884   doi:10.1016/j.icarus.2012.02.034

885 Carrasco, N., Giuliani, A., Correia, J.J., Cernogora, G., 2013. VUV photochemistry simulation of

886   planetary upper atmosphere using synchrotron radiation. J. Synchrotron Radiat. 20, 587–
887   589. doi:10.1107/S0909049513013538

888   Carrasco, N., Hébrard, E., Banaszkiewicz, M., Dobrijevic, M., Pernot, P., 2007. Influence of
889   neutral transport on ion chemistry uncertainties in Titan ionosphere. Icarus 192, 519–526.
890   doi:10.1016/j.icarus.2007.08.016

891   Carruth, G., Kobayashi, R., 1973. Vapor Pressure of Normal Paraffins Ethane Through n-
892   Decane from Their Triple Points to About 10Mm Hg. J. Chem. Eng. 18, 115–126.
893   doi:10.1021/je60057a009

894   Chang, J.S., Lawless, P.A., Yamamoto, T., 1991. Corona Discharge Processes. IEEE Trans.
895   Plasma Sci. 19, 1152–1166. doi:10.1109/27.125038

896   Cicerone, R.J., Zellner, R., 1983. The atmospheric chemistry of hydrogen cyanide (HCN). J.
897   Geophys. Res. 88, 10689. doi:10.1029/JC088iC15p10689

898   Coll, P., Coscia, D., Smith, N., Gazeau, M.-C., Ramírez, S.I., Cernogora, G., Israël, G., Raulin,
899   F., 1999. Experimental laboratory simulation of Titan's atmosphere: aerosols and gas
900   phase. Planet. Space Sci. 47, 1331–1340. doi:10.1016/S0032-0633(99)00054-9

901   Cordiner, M.A., Nixon, C.A., Teanby, N.A., Serigano, J., Charnley, S.B., Milam, S.N., Mumma,
902   M.J., Irwin, P.G.J., Lis, D.C., Villanueva, G., Paganini, L., Kuan, Y.-J., Remijan, A.J.,
903   2014a. ALMA measurements of the HNC and HC_3N distributions in Titan's atmosphere
904   2–7. doi:10.1088/2041-8205/795/2/L30

905   Cordiner, M.A., Palmer, M.Y., Nixon, C.A., Irwin, P.G.J., Teanby, N.A., Charnley, S.B., Mumma,
906   M.J., Kisiel, Z., Serigano, J., Kuan, Y.-J., Chuang, Y.-L., Wang, K.-S., 2014b. Ethyl cyanide
907   on Titan: Spectroscopic detection and mapping using ALMA 3–8. doi:10.1088/2041-
908   8205/800/1/L14

909   Courtin, R., Swinyard, B.M., Moreno, R., Fulton, T., Lellouch, E., Rengel, M., Hartogh, P., 2011.
910   First results of Herschel -SPIRE observations of Titan. Astron. Astrophys. 536, L2.
911   doi:10.1051/0004-6361/201118304

912   Coustenis, A., Achterberg, R.K., Conrath, B.J., Jennings, D.E., Marten, A., Gautier, D., Nixon,
913   C.A., Flasar, F.M., Teanby, N.A., Bézard, B., Samuelson, R.E., Carlson, R.C., Lellouch, E.,
914   Bjoraker, G.L., Romani, P.N., Taylor, F.W., Irwin, P.G.J., Fouchet, T., Hubert, A., Orton,
915   G.S., Kunde, V.G., Vinatier, S., Mondellini, J., Abbas, M.M., Courtin, R., 2007. The
916   composition of Titan's stratosphere from Cassini/CIRS mid-infrared spectra. Icarus 189,
917   35–62. doi:10.1016/j.icarus.2006.12.022

918   Coustenis, A., Jennings, D.E., Achterberg, R.K., Bampasidis, G., Lavvas, P., Nixon, C.A.,
919   Teanby, N.A., Anderson, C.M., Cottini, V., Flasar, F.M., 2016. Titan's temporal evolution in

920   stratospheric trace gases near the poles. Icarus 270, 409–420.
921   doi:10.1016/j.icarus.2015.08.027

922 Coustenis, A., Salama, A., Schulz, B., Ott, S., Lellouch, E., Encrenaz, T., Gautier, D.,
923   Feuchtgruber, H., 2003. Titan's atmosphere from ISO mid-infrared spectroscopy. Icarus
924   161, 383–403. doi:10.1016/S0019-1035(02)00028-3

925 Crary, F.J., Magee, B.A., Mandt, K., Waite, J.H., Westlake, J., Young, D.T., 2009. Heavy ions,
926   temperatures and winds in Titan's ionosphere: Combined Cassini CAPS and INMS
927   observations. Planet. Space Sci. 57, 1847–1856. doi:10.1016/j.pss.2009.09.006

928 Crespin, A., Lebonnois, S., Hourdin, F., Rannou, P., 2005. Seasonal variations of Titan's
929   stratospheric composition in the LMD/SA Global ClimateModel. Bull. Am. Astron. Soc. 37,
930   718.

931 Cui, J., Galand, M., Yelle, R. V, Vuitton, V., Wahlund, J., Lavvas, P.P., 2009. Diurnal variations
932   of Titan's ionosphere. J. Geophys. Res. 114, 1–20. doi:10.1029/2009JA014228

933 Cui, J., Yelle, R. V., Vuitton, V., Waite, J.H., Kasprzak, W.T., Gell, D.A., Niemann, H.B., Müller-
934   Wodarg, I.C.F., Borggren, N., Fletcher, G.G., Patrick, E.L., Raaen, E., Magee, B.A., 2009.
935   Analysis of Titan's neutral upper atmosphere from Cassini Ion Neutral Mass Spectrometer
936   measurements. Icarus 200, 581–615. doi:10.1016/j.icarus.2008.12.005

937 Davis, D.D., Okabe, H., 1968. Determination of Bond Dissociation Energies in Hydrogen
938   Cyanide. Cyanogen and Cyanogen Halides by the Photodissociation Method. J. Chem.
939   Phys. 49, 5526. doi:10.1063/1.1670082

940 de Kok, R.J., Teanby, N.A., Maltagliati, L., Irwin, P.G.J., Vinatier, S., 2014. HCN ice in Titan's
941   high-altitude southern polar cloud. Nature 514, 65–7. doi:10.1038/nature13789

942 Desai, R.T., Coates, A.J., Wellbrock, A., Vuitton, V., Crary, F.J., González-Caniulef, D.,
943   Shebanits, O., Jones, G.H., Lewis, G.R., Waite, J.H., Taylor, S.A., Kataria, D.O., Wahlund,
944   J.-E., Edberg, N.J.T., Sittler, E.C., 2017. Carbon chain anions and the growth of complex
945   organic molecules in Titan's ionosphere. Astrophys. J. Lett. 844, 1–8. doi:10.3847/2041-
946   8213/aa7851

947 Doose, L.R., Karkoschka, E., Tomasko, M.G., Anderson, C.M., 2016. Vertical structure and
948   optical properties of Titan's aerosols from radiance measurements made inside and
949   outside the atmosphere. Icarus 270, 355–375. doi:10.1016/j.icarus.2015.09.039

950 English, M.A., Lara, L.M., Lorenz, R.D., Ratcliff, P.R., Rodrigo, R., 1996. Ablation and chemistry
951   of meteoric materials in the atmosphere of Titan. Adv. Sp. Res. 17, 157–160.
952   doi:10.1016/0273-1177(95)00774-9

953 Flasar, F.M., Achterberg, R.K., Conrath, B.J., Gierasch, P.J., Kunde, V.G., Nixon, C.A.,

954   Bjoraker, G.L., Jennings, D.E., Romani, P.N., Simon-Miller, A.A., Bezard, B., Coustenis, A.,

955   Irwin, P.G.J., Teanby, N.A., Brasunas, J., Pearl, J.C., Segura, M.E., Carlson, R.C.,

956   Mamoutkine, A., Schinder, P.J., Barucci, A., Courtin, R., Fouchet, T., Gautier, D., Lellouch,

957   E., Marten, A., Prange, R., Vinatier, S., Strobel, D.F., Calcutt, S.B., Read, P.L., Taylor,

958   F.W., Bowles, N., Samuelson, R.E., Orton, G.S., Spilker, L.J., Owen, T.C., Spencer, J.R.,

959   Showalter, M.R., Ferrari, C., Abbas, M.M., Raulin, F., Edgington, S., Ade, P., Wishnow,

960   E.H., 2005. Titan's Atmospheric Temperatures, Winds, and Composition. Science (80-.).

961   308, 975–978. doi:10.1126/science.1111150

962 Frankland, V.L., James, A.D., Sánchez, J.D.C., Mangan, T.P., Willacy, K., Poppe, A.R., Plane,

963   J.M.C., 2016. Uptake of acetylene on cosmic dust and production of benzene in Titan's

964   atmosphere. Icarus 278, 88–99. doi:10.1016/j.icarus.2016.06.007

965 Fray, N., Schmitt, B., 2009. Sublimation of ices of astrophysical interest: A bibliographic review.

966   Planet. Space Sci. 57, 2053–2080. doi:10.1016/j.pss.2009.09.011

967 Gautier, T., Carrasco, N., Buch, A., Szopa, C., Sciamma-O'Brien, E., Cernogora, G., 2011.

968   Nitrile gas chemistry in Titan's atmosphere. Icarus 213, 625–635.

969   doi:10.1016/j.icarus.2011.04.005

970 Gautier, T., Carrasco, N., Schmitz-Afonso, I., Touboul, D., Szopa, C., Buch, A., Pernot, P.,

971   2014. Nitrogen incorporation in titan's tholins inferred by high resolution orbitrap mass

972   spectrometry and gas chromatography-mass spectrometry. Earth Planet. Sci. Lett. 404,

973   33–42. doi:10.1016/j.epsl.2014.07.011

974 Hanel, R., Conrath, B., Flasar, F.M., Kunde, V.G., Maguire, W.C., Pearl, J., Pirraglia, J.,

975   Samuelson, R.E., Herath, L., Allison, M., Cruikshank, D., Gautier, D., Gierasch, P., Horn,

976   L., Koppany, R., Ponnamperuma, C., 1981. Infrared Observations of the Saturnian System

977   from Voyager 1. Science (80-.). 212, 192–200. doi:10.1126/science.212.4491.192

978 Harris, G.J., Tennyson, J., Kaminsky, B.M., Pavlenko, Y. V., Jones, H.R.A., 2006. Improved

979   HCN/HNC linelist, model atmospheres and synthetic spectra for WZ Cas. Mon. Not. R.

980   Astron. Soc. 367, 400–406. doi:10.1111/j.1365-2966.2005.09960.x

981 He, C., Smith, M.A., 2014. Identification of nitrogenous organic species in Titan aerosols

982   analogs: Implication for prebiotic chemistry on Titan and early Earth. Icarus 238, 86–92.

983   doi:10.1016/j.icarus.2014.05.012

984 Hidayat, T., Marten, A., Bézard, B., Gautier, D., Owen, T.C., Matthews, H.E., Paubert, G., 1997.

985   Millimeter and Submillimeter Heterodyne Observations of Titan : Retrieval of the Vertical

986   Profile of HCN and the 12 C / 13 C Ratio 182, 170–182.

987 Hill, C., Yurchenko, S.N., Tennyson, J., 2013. Temperature-dependent molecular absorption

988   cross sections for exoplanets and other atmospheres. Icarus 226, 1673–1677.
989   doi:10.1016/j.icarus.2012.07.028

990 Hörst, S.M., 2017. Titan's Atmosphere and Climate. J. Geophys. Res. Planets 432–482.
991   doi:10.1002/2016JE005240

992 Hörst, S.M., Yelle, R.V., Buch, A., Carrasco, N., Cernogora, G., Dutuit, O., Quirico, E.,
993   Sciamma-O'Brien, E., Smith, M. a., Somogyi, Á., Szopa, C., Thissen, R., Vuitton, V., 2012.
994   Formation of Amino Acids and Nucleotide Bases in a Titan Atmosphere Simulation
995   Experiment. Astrobiology 12, 809–817. doi:10.1089/ast.2011.0623

996 Hörst, S.M., Yoon, Y.H., Ugelow, M.S., Parker, A.H., Li, R., de Gouw, J.A., Tolbert, M.A., 2018.
997   Laboratory investigations of Titan haze formation: In situ measurement of gas and particle
998   composition. Icarus 301, 136–151. doi:10.1016/j.icarus.2017.09.039

999 Israel, G.L., Szopa, C., Raulin, F., Cabane, M., Niemann, H.B., Atreya, S.K., Bauer, S.J., Brun,
1000   J.-F., Chassefière, E., Coll, P., Condé, E., Coscia, D., Hauchecorne, a, Millian, P.,
1001   Nguyen, M.-J., Owen, T., Riedler, W., Samuelson, R.E., Siguier, J.-M., Steller, M.,
1002   Sternberg, R., Vidal-Madjar, C., 2005. Complex organic matter in Titan's atmospheric
1003   aerosols from in situ pyrolysis and analysis. Nature 438, 796–799.
1004   doi:10.1038/nature04349

1005 Johnson, R.E., Tucker, O.J., Volkov, A.N., 2016. Evolution of an early Titan atmosphere. Icarus
1006   271, 202–206. doi:10.1016/j.icarus.2016.01.014

1007 Khare, B., Sagan, C., 1973. Red clouds in reducing atmospheres. Icarus 20, 311–321.
1008   doi:10.1016/0019-1035(73)90008-0

1009 Khare, B.N., Sagan, C., Arakawa, E.T., Suits, F., Callcott, T.A., Williams, M.W., 1984. Optical
1010   constants of organic tholins produced in a simulated Titanian atmosphere: From soft x-ray
1011   to microwave frequencies. Icarus 60, 127–137. doi:10.1016/0019-1035(84)90142-8

1012 Khare, B.N., Sagan, C., Zumberge, J.E., Sklarew, D.S., Nagy, B., 1981. Organic solids
1013   produced by electrical discharge in reducing atmospheres: Tholin molecular analysis.
1014   Icarus 48, 290–297. doi:10.1016/0019-1035(81)90110-X

1015 Kim, S.J., Geballe, T.R., Noll, K.S., Courtin, R., 2005. Clouds, haze, and CH4, CH3D, HCN, and
1016   C2 H2 in the atmosphere of Titan probed via 3 ??m spectroscopy. Icarus 173, 522–532.
1017   doi:10.1016/j.icarus.2004.09.006

1018 Krasnopolsky, V.A., 2009. A photochemical model of Titan's atmosphere and ionosphere. Icarus
1019   201, 226–256. doi:10.1016/j.icarus.2008.12.038

1020 Kunde, V.G., Aikin, A.C., Hanel, R.A., Jennings, D.E., Maguire, W.C., Samuelson, R.E., 1981.
1021   C4H2, HC3N and C2N2 in Titan's atmosphere. Nature 292, 686–688.

1022   doi:10.1038/292686a0

1023   Lara, L.M., Lellouch, E., López-Moreno, J.J., Rodrigo, R., 1996. Vertical distribution of Titan's
1024   atmospheric neutral constituents. J. Geophys. Res. 101, 23261. doi:10.1029/96JE02036

1025   Largo, L., Redondo, P., Rayón, V.M., Largo, A., Barrientos, C., 2010. The reaction between NH
1026   + and CH 3 COOH : a possible process for the formation of glycine precursors in the
1027   interstellar medium. Astron. Astrophys. 516, A79. doi:10.1051/0004-6361/201014057

1028   Loison, J.C., Hébrard, E., Dobrijevic, M., Hickson, K.M., Caralp, F., Hue, V., Gronoff, G., Venot,
1029   O., Bénilan, Y., 2015. The neutral photochemistry of nitriles, amines and imines in the
1030   atmosphere of Titan. Icarus 247, 218–247. doi:10.1016/j.icarus.2014.09.039

1031   Maguire, W.C., Hanel, R.A., Jennings, D.E., Kunde, V.G., Samuelson, R.E., 1981. C3H8 and
1032   C3H4 in Titan's atmosphere. Nature 292, 683–686. doi:10.1038/292683a0

1033   Mahjoub, A., Carrasco, N., Dahoo, P.R., Fleury, B., Gautier, T., Cernogora, G., 2014. Effect of
1034   the synthesis temperature on the optical indices of organic materials produced by N2-CH4
1035   RF plasma. Plasma Process. Polym. 11, 409–417. doi:10.1002/ppap.201300150

1036   Maurice, S., Sittler, E.C., Cooper, J.F., Mauk, B.H., Blanc, M., Selesnick, R.S., 1996.
1037   Comprehensive analysis of electron observations at Saturn: Voyager 1 and 2. J. Geophys.
1038   Res. 101.

1039   McKay, C.P., 1996. Elemental composition, solubility, and optical properties of Titan's organic
1040   haze. Planet. Space Sci. 44, 741–747. doi:10.1016/0032-0633(96)00009-8

1041   Molter, E.M., Nixon, C.A., Cordiner, M.A., Serigano, J., Irwin, P.G.J., Teanby, N.A., Charnley,
1042   S.B., Lindberg, J.E., 2016. ALMA Observations of HCN and its Isotopologues on Titan 1–
1043   14.

1044   Moreno, R., Lellouch, E., Vinatier, S., Gurwell, M., Moullet, A., Lara, L.M., Hidayat, T., 2015.
1045   ALMA observations of Titan : Vertical and spatial distribution of nitriles. EPSC 2015 10,
1046   2015.

1047   Neish, C.D., Somogyi, Á., Lunine, J.I., Smith, M.A., 2009. Low temperature hydrolysis of
1048   laboratory tholins in ammonia-water solutions: Implications for prebiotic chemistry on Titan.
1049   Icarus 201, 412–421. doi:10.1016/j.icarus.2009.01.003

1050   Nelson, R.M., Kamp, L.W., Matson, D.L., Irwin, P.G.J., Baines, K.H., Boryta, M.D., Leader, F.E.,
1051   Jaumann, R., Smythe, W.D., Sotin, C., Clark, R.N., Cruikshank, D.P., Drossart, P., Pearl,
1052   J.C., Hapke, B.W., Lunine, J., Combes, M., Bellucci, G., Bibring, J.P., Capaccioni, F.,
1053   Cerroni, P., Coradini, A., Formisano, V., Filacchione, G., Langevin, R.Y., McCord, T.B.,
1054   Mennella, V., Nicholson, P.D., Sicardy, B., 2009. Saturn's Titan: Surface change,
1055   ammonia, and implications for atmospheric and tectonic activity. Icarus 199, 429–441.

1056   doi:10.1016/j.icarus.2008.08.013

1057 Nixon, C.A., Achterberg, R.K., Ádámkovics, M., Bézard, B., Bjoraker, G.L., Cornet, T., Hayes,
1058   A.G., Lellouch, E., Lemmon, M.T., López-Puertas, M., Rodriguez, S., Sotin, C., Teanby,
1059   N.A., Turtle, E.P., West, R.A., 2016. Titan Science with the James Webb Space Telescope.
1060   Astron. Soc. Pacific 128, 1–28. doi:10.1088/1538-3873/128/959/018009

1061 Oró, J., 1961. Comets and the Formation of Biochemical Compounds on the Primitive Earth.
1062   Nature 189, 775–776.

1063 Palmer, M.Y., Cordiner, M.A., Nixon, C.A., Charnley, S.B., Teanby, N.A., Kisiel, Z., Irwin, P.G.J.,
1064   Mumma, M.J., 2017. ALMA detection and astrobiological potential of vinyl cyanide on Titan
1065   1–7.

1066 Paubert, G., Gautier, D., Courtin, R., 1984. The millimeter spectrum of Titan: Detectability of
1067   HCN, HC3N, and CH3CN and the CO abundance. Icarus 60, 599–612. doi:10.1016/0019-
1068   1035(84)90167-2

1069 Peng, Z., Gautier, T., Carrasco, N., Pernot, P., Giuliani, A., Mahjoub, A., Correia, J.-J., Buch, A.,
1070   Bénilan, Y., Szopa, C., Cernogora, G., 2013. Titan's atmosphere simulation experiment
1071   using continuum UV-VUV synchrotron radiation. J. Geophys. Res. Planets 118, 778–788.
1072   doi:10.1002/jgre.20064

1073 Pernot, P., Carrasco, N., Thissen, R., Schmitz-Afonso, I., 2010. Tholinomics—Chemical
1074   Analysis of Nitrogen-Rich Polymers. Anal. Chem. 82, 1371–1380. doi:10.1021/ac902458q

1075 Pintassilgo, C.D., Loureiro, J., Cernogora, G., Touzeau, M., 1999. Methane decomposition and
1076   active nitrogen in a N2-CH4 glow discharge at low pressures. Plasma Sources Sci.
1077   Technol. 463–478. doi:http://dx.doi.org/10.1016/0019-1035(91)90068-5

1078 Rahm, M., Lunine, J.I., Usher, D.A., Shalloway, D., 2016. Polymorphism and electronic structure
1079   of polyimine and its potential significance for prebiotic chemistry on Titan 1–6.
1080   doi:10.1073/pnas.1606634113

1081 Rengel, M., Sagawa, H., Hartogh, P., Lellouch, E., Feuchtgruber, H., Moreno, R., Jarchow, C.,
1082   Courtin, R., Cernicharo, J., Lara, L.M., 2014. Herschel/PACS spectroscopy of trace gases
1083   of the stratosphere of Titan. Astron. Astrophys. 561, A4. doi:10.1051/0004-
1084   6361/201321945

1085 Sagan, C., 1973. The greenhouse of Titan. Icarus 18, 649–656. doi:10.1016/0019-
1086   1035(73)90068-7

1087 Sagan, C., Reid Thompson, W., 1984. Production and condensation of organic gases in the
1088   atmosphere of Titan. Icarus 59, 133–161. doi:10.1016/0019-1035(84)90018-6

1089 Sciamma-O'Brien, E., Carrasco, N., Szopa, C., Buch, A., Cernogora, G., 2010. Titan's

1090   atmosphere: An optimal gas mixture for aerosol production? Icarus 209, 704–714.
1091   doi:10.1016/j.icarus.2010.04.009

1092 Sciamma-O'Brien, E., Upton, K.T., Beauchamp, J.L., Salama, F., 2015. The THS experiment:
1093   Simulating Titan's atmospheric chemistry at low temperature (200 K). Proc. Int. Astron.
1094   Union 11, 327–328. doi:10.1017/S1743921316003197

1095 Serigano, J., Nixon, C.A., Cordiner, M.A., Irwin, P.G.J., Teanby, N.A., Charnley, S.B., Lindberg,
1096   J.E., 2016. Isotopic Ratios of Carbon and Oxygen in Titan's CO using ALMA. Astrophys. J.
1097   Lett. 821, 1–6. doi:10.3847/2041-8205/821/1/L8

1098 Sharpe, S.N., Johnson, T.J., James, R.L., Chu, P.M., Rhoderick, G.C., Johnson, P. a., 2004.
1099   Gas Phase Database for Quantitative Infrared Spectroscopy. Appl. Spectrosc. 58, 1452–
1100   1461. doi:10.1366/0003702042641281

1101 Sittler, E.C., Ali, A., Cooper, J.F., Hartle, R.E., Johnson, R.E., Coates, A.J., Young, D.T., 2009.
1102   Heavy ion formation in Titan's ionosphere: Magnetospheric introduction of free oxygen and
1103   a source of Titan's aerosols? Planet. Space Sci. 57, 1547–1557.
1104   doi:10.1016/j.pss.2009.07.017

1105 Sittler, E.C., Ogilvie, K.W., Scudder, J.D., 1983. Survey of low-energy plasma electrons in
1106   Saturn's magnetosphere: Voyagers 1 and 2. J. Geophys. Res. 88, 8847.
1107   doi:10.1029/JA088iA11p08847

1108 Snowden, D., Yelle, R. V, Cui, J., Wahlund, J., Edberg, N.J.T., Ågren, K., 2013. The thermal
1109   structure of Titan's upper atmosphere, I: Temperature profiles from Cassini INMS
1110   observations. Icarus 226, 552–582. doi:10.1016/j.icarus.2013.06.006

1111 Szopa, C., Cernogora, G., Boufendi, L., Correia, J.J., Coll, P., 2006. PAMPRE: A dusty plasma
1112   experiment for Titan's tholins production and study. Planet. Space Sci. 54, 394–404.
1113   doi:10.1016/j.pss.2005.12.012

1114 Tanguy, L., Zard, B.B.I., Marten, A., Gautier, D., Rard, E.G.I., Paubert, G., Lecacheux, A., 1990.
1115   Stratospheric Profile of HCN on Titan from Millimeter Observations 57.

1116 Teanby, N.A., Irwin, P.G.J., de Kok, R., Vinatier, S., Bézard, B., Nixon, C.A., Flasar, F.M.,
1117   Calcutt, S.B., Bowles, N.E., Fletcher, L., Howett, C., Taylor, F.W., 2007. Vertical profiles of
1118   HCN, HC3N, and C2H2 in Titan's atmosphere derived from Cassini/CIRS data. Icarus 186,
1119   364–384. doi:10.1016/j.icarus.2006.09.024

1120 Teanby, N.A., Irwin, P.G.J., Nixon, C.A., De Kok, R., Vinatier, S., Coustenis, A., Sefton-Nash,
1121   E., Calcutt, S.B., Flasar, F.M., 2012. Active upper-atmosphere chemistry and dynamics
1122   from polar circulation reversal on Titan. Nature 491, 732–735. doi:10.1038/nature11611

1123 Teanby, N. a, Irwin, P.G.J., de Kok, R., Nixon, C. a, 2009. Dynamical implications of seasonal

1124   and spatial variations in Titan's stratospheric composition. Philos. Trans. A. Math. Phys.
1125   Eng. Sci. 367, 697–711. doi:10.1098/rsta.2008.0164

1126 Tennyson, J., Yurchenko, S.N., Al-refaie, A.F., Emma, J., Chubb, K.L., Coles, P.A.,
1127   Diamantopoulou, S., Maire, N., Hill, C., Lam, A.Z., Lodi, L., Mckemmish, L.K., Na, Y.,
1128   Owens, A., Polyansky, O.L., Sousa-silva, C., Daniel, S., Yachmenev, A., Zak, E., 2016.
1129   The ExoMol database: molecular line lists for exoplanet and other hot atmospheres. J. Mol.
1130   Spectrosc. 1–68.

1131 Tigrine, S., Carrasco, N., Vettier, L., Cernogora, G., 2016. A microwave plasma source for VUV
1132   atmospheric photochemistry. J. Phys. D. Appl. Phys. 49, 395202. doi:10.1088/0022-
1133   3727/49/39/395202

1134 Vinatier, S., Bézard, B., de Kok, R., Anderson, C.M., Samuelson, R.E., Nixon, C.A.,
1135   Mamoutkine, A., Carlson, R.C., Jennings, D.E., Guandique, E.A., Bjoraker, G.L., Michael
1136   Flasar, F., Kunde, V.G., 2009. Analysis of Cassini/CIRS limb spectra of Titan acquired
1137   during the nominal mission I: Hydrocarbons, nitriles and CO_2 vertical mixing ratio profiles.
1138   Icarus 210, 852–866. doi:10.1016/j.icarus.2010.06.024

1139 Vinatier, S., Bézard, B., Fouchet, T., Teanby, N.A., de Kok, R., Irwin, P.G.J., Conrath, B.J.,
1140   Nixon, C.A., Romani, P.N., Flasar, F.M., Coustenis, A., 2007. Vertical abundance profiles
1141   of hydrocarbons in Titan's atmosphere at 15° S and 80° N retrieved from Cassini/CIRS
1142   spectra. Icarus 188, 120–138. doi:10.1016/j.icarus.2006.10.031

1143 Vinatier, S., Bézard, B., Lebonnois, S., Teanby, N.A., Achterberg, R.K., Gorius, N., Mamoutkine,
1144   A., Guandique, E., Jolly, A., Jennings, D.E., Flasar, F.M., 2015. Seasonal variations in
1145   Titan's middle atmosphere during the northern spring derived from Cassini/CIRS
1146   observations. Icarus 250, 95–115. doi:10.1016/j.icarus.2014.11.019

1147 Vuitton, V., Yelle, R. V., McEwan, M.J., 2007. Ion chemistry and N-containing molecules in
1148   Titan's upper atmosphere. Icarus 191, 722–742. doi:10.1016/j.icarus.2007.06.023

1149 Waite, J.H., Niemann, H.B., Yelle, R. V., Kasprzak, W.T., Cravens, T.E., Luhmann, J.G.,
1150   McNutt, R.L., Ip, W.H., Gell, D., De La Haye, V., Muller-Wordag, I., Magee, B.A., Borggren,
1151   N., Ledvina, S.A., Fletcher, G.G., Walter, E.M., Miller, R., Scherer, S., Thorpe, R.L., Xu, X.,
1152   Block, B.P., Arnett, K., 2005. Ion Neutral Mass Spectrometer Results from the First Flyby of
1153   Titan. Science (80-.). 85, 195–209. doi:10.1016/S0022-4073(03)00225-5

1154 Waite, J.H., Young, D.T., Cravens, T.E., Coates, A.J., Crary, F.J., Magee, B., Westlake, J.,
1155   2007. The Process of Tholin Formation in Titan's Upper Atmosphere. Science (80-.). 870.
1156   doi:10.1126/science.1139727

1157 Wellbrock, A., Coates, A.J., Jones, G.H., Lewis, G.R., Waite, J.H., 2013. Cassini CAPS-ELS

1158   observations of negative ions in Titan's ionosphere: Trends of density with altitude.

1159   Geophys. Res. Lett. 40, 4481–4485. doi:10.1002/grl.50751

1160 Wilson, E.H., Atreya, S.K., 2004. Current state of modeling the photochemistry of Titan's

1161   mutually dependent atmosphere and ionosphere. J. Geophys. Res. E Planets 109.

1162   doi:10.1029/2003JE002181

1163 Wilson, E.H., Atreya, S.K., 2003. Chemical sources of haze formation in Titan's atmosphere.

1164   Planet. Space Sci. 51, 1017–1033. doi:10.1016/j.pss.2003.06.003

1165 Yelle, R. V, Vuitton, V., Lavvas, P., Klippenstein, S.J., Smith, M. a, Hörst, S.M., Cui, J., 2010.

1166   Formation of NH3 and CH2NH in Titan's upper atmosphere. Faraday Discuss. 147, 31.

1167   doi:10.1039/c004787m

1168

1169

1170

1171

1172

1173

1174

1175

1176

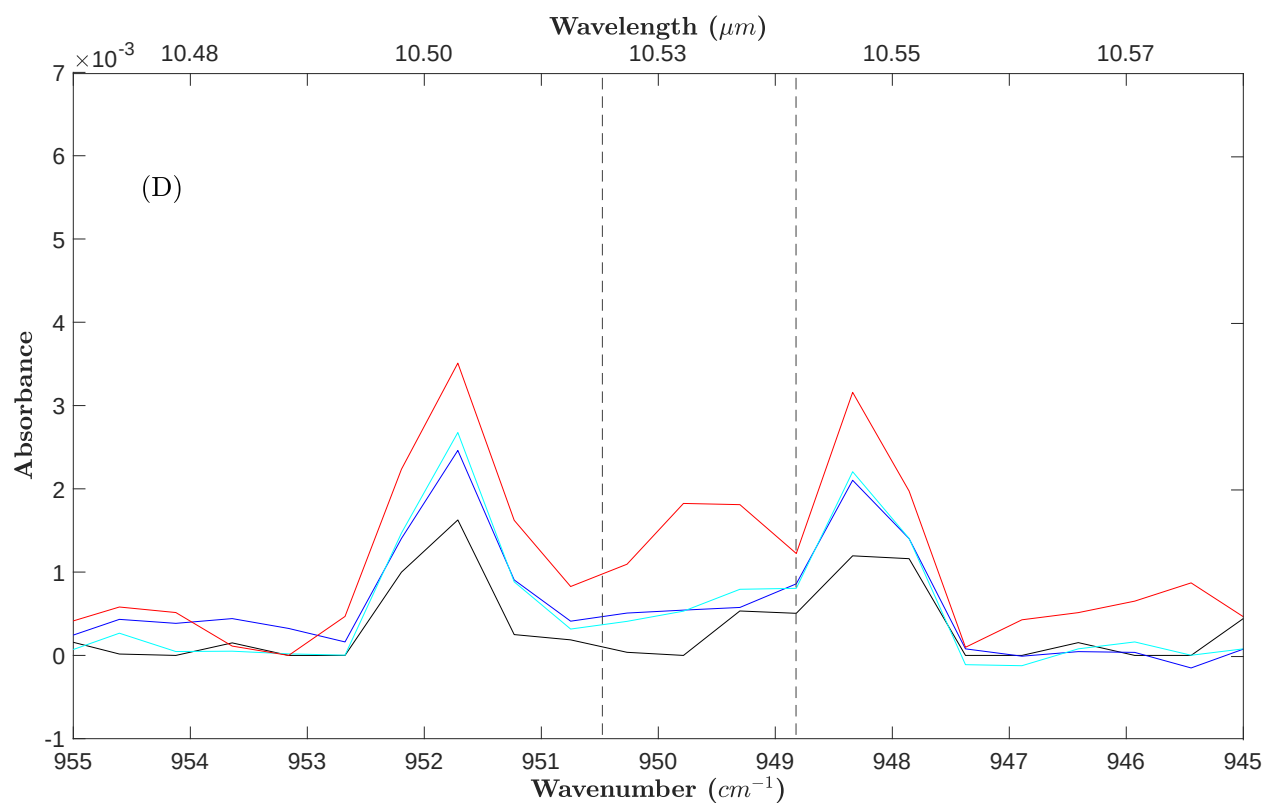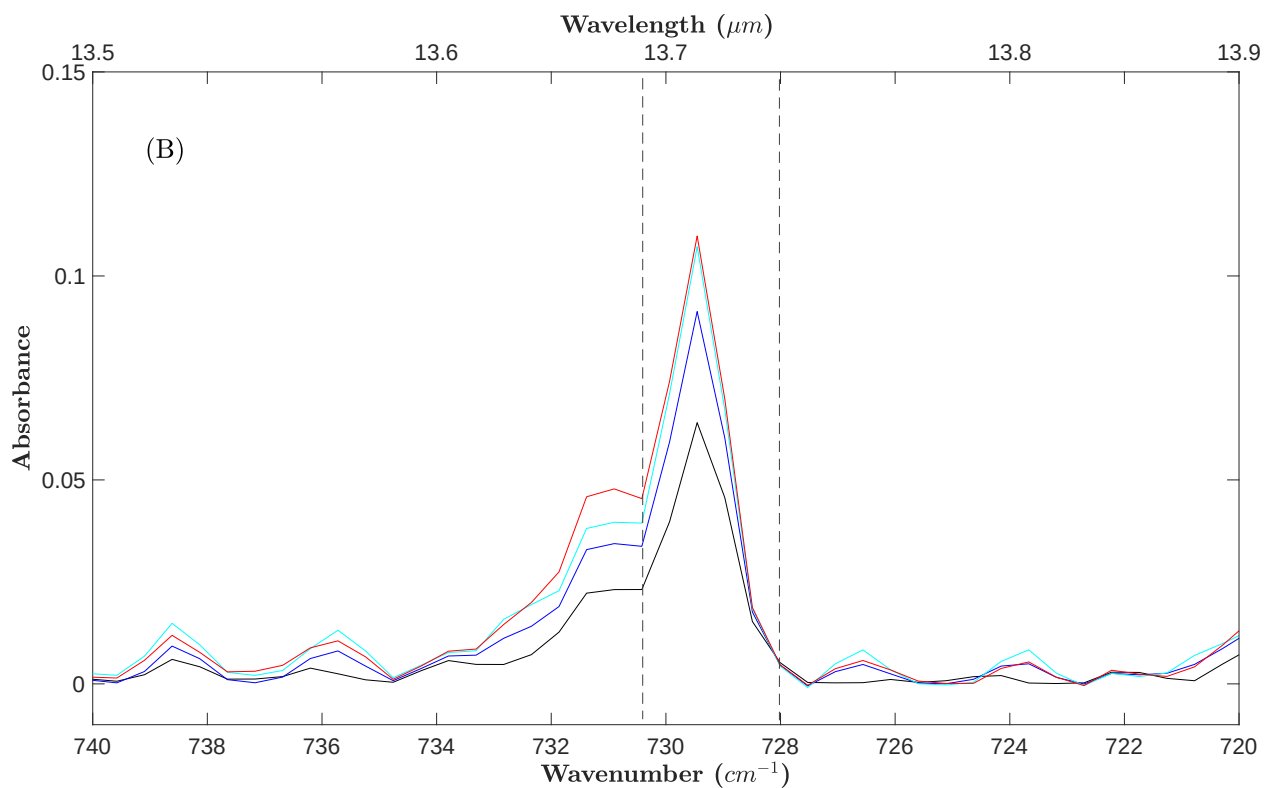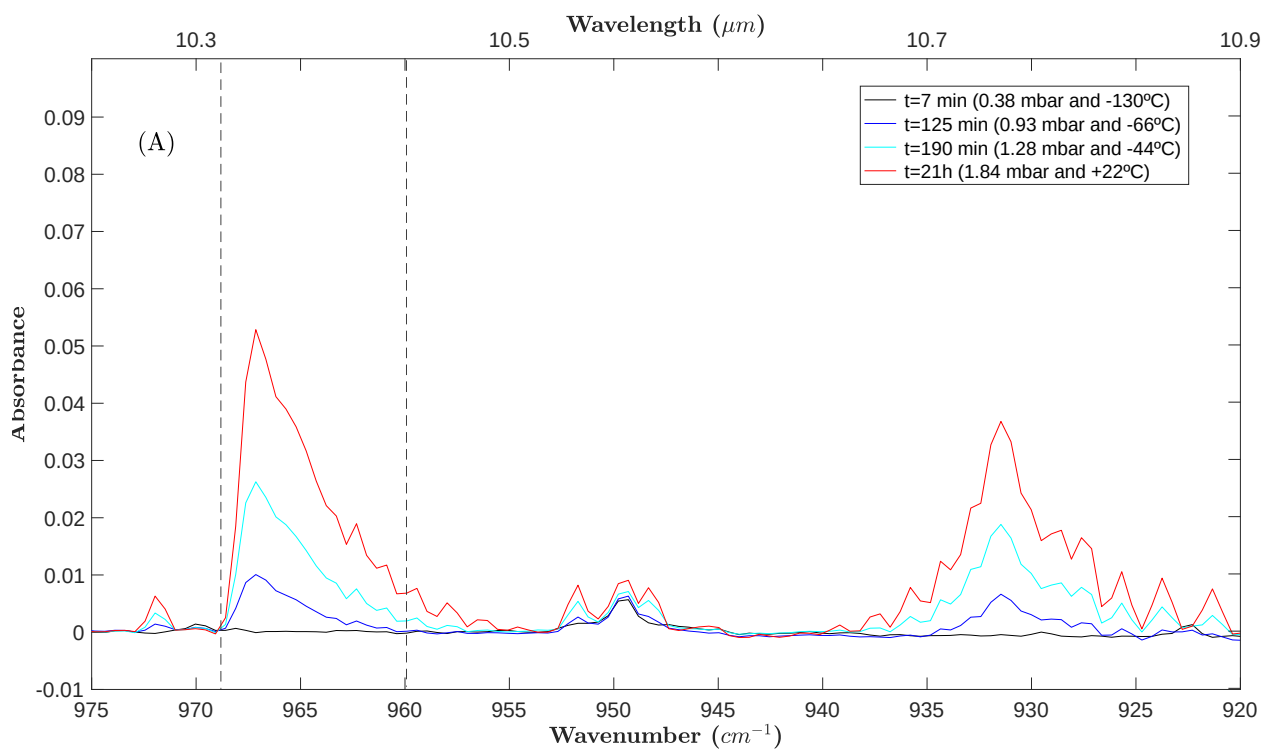1177

1178

1179

1180

1181

1182

1% CH$_4$
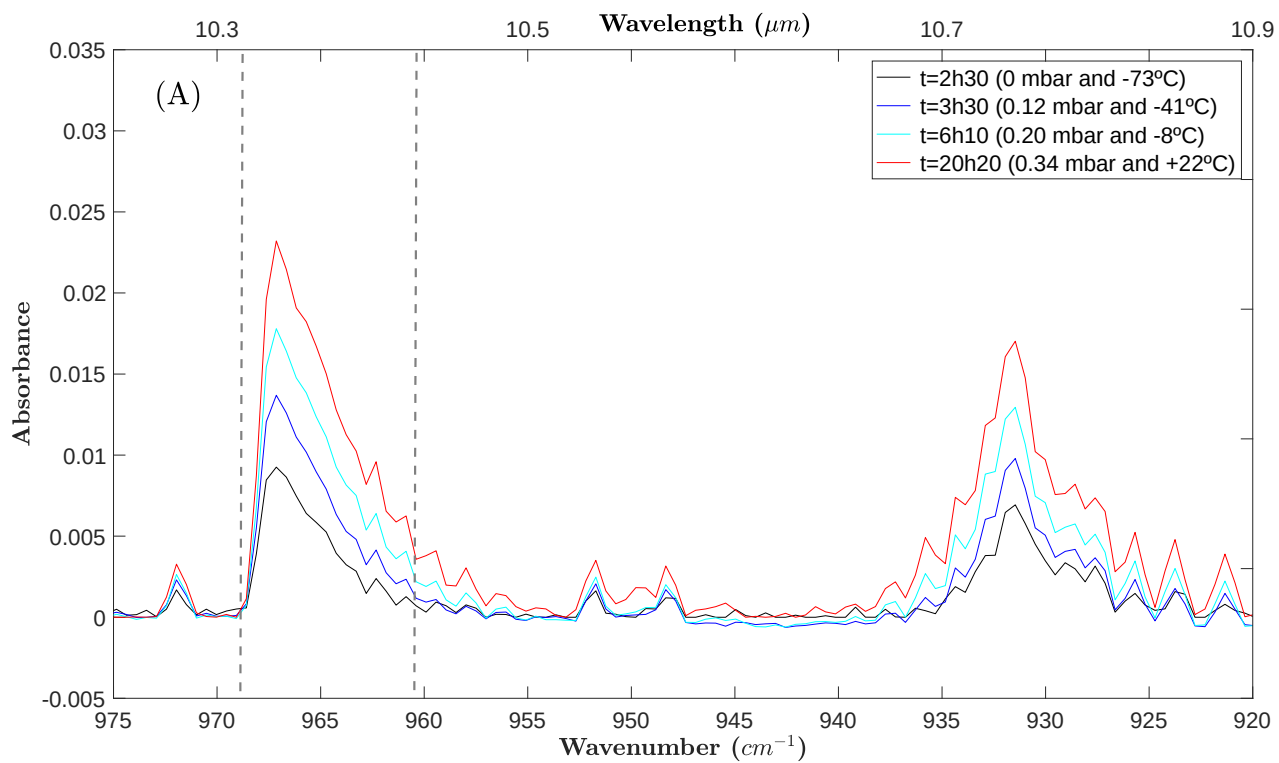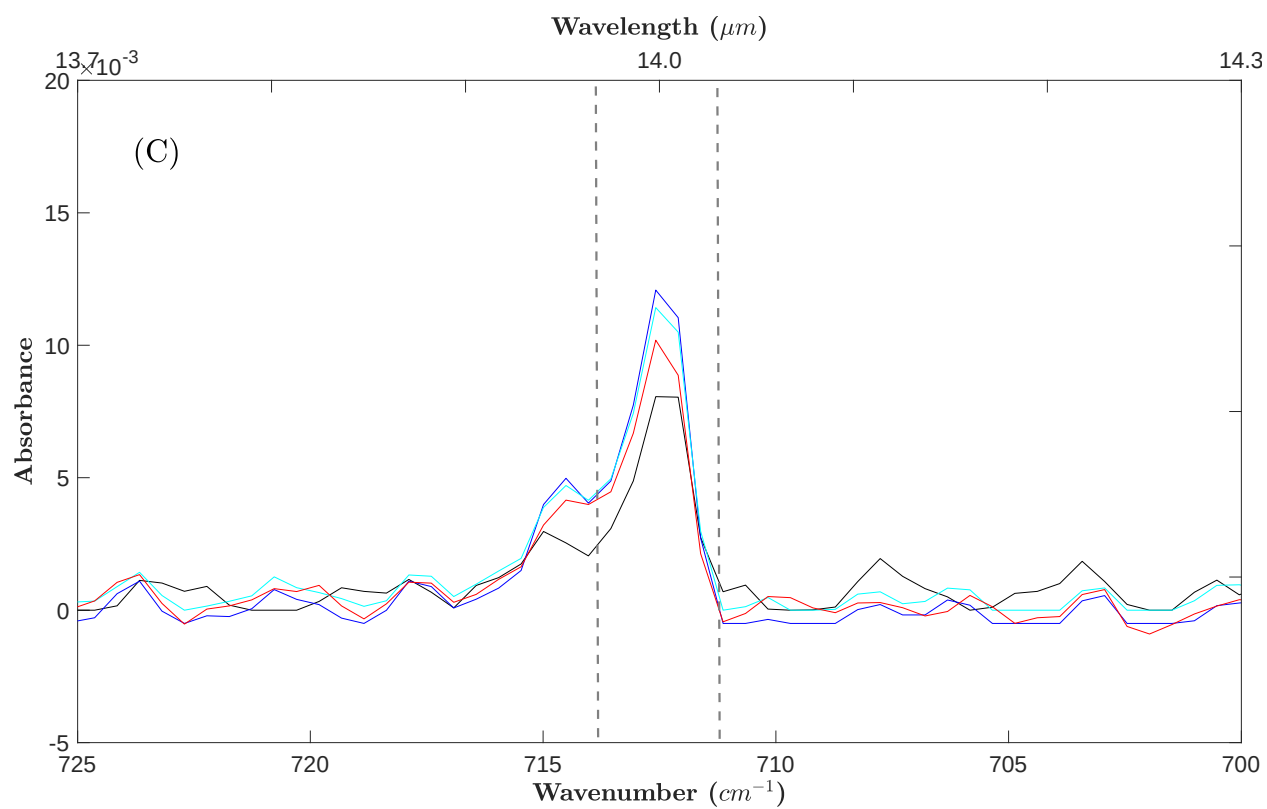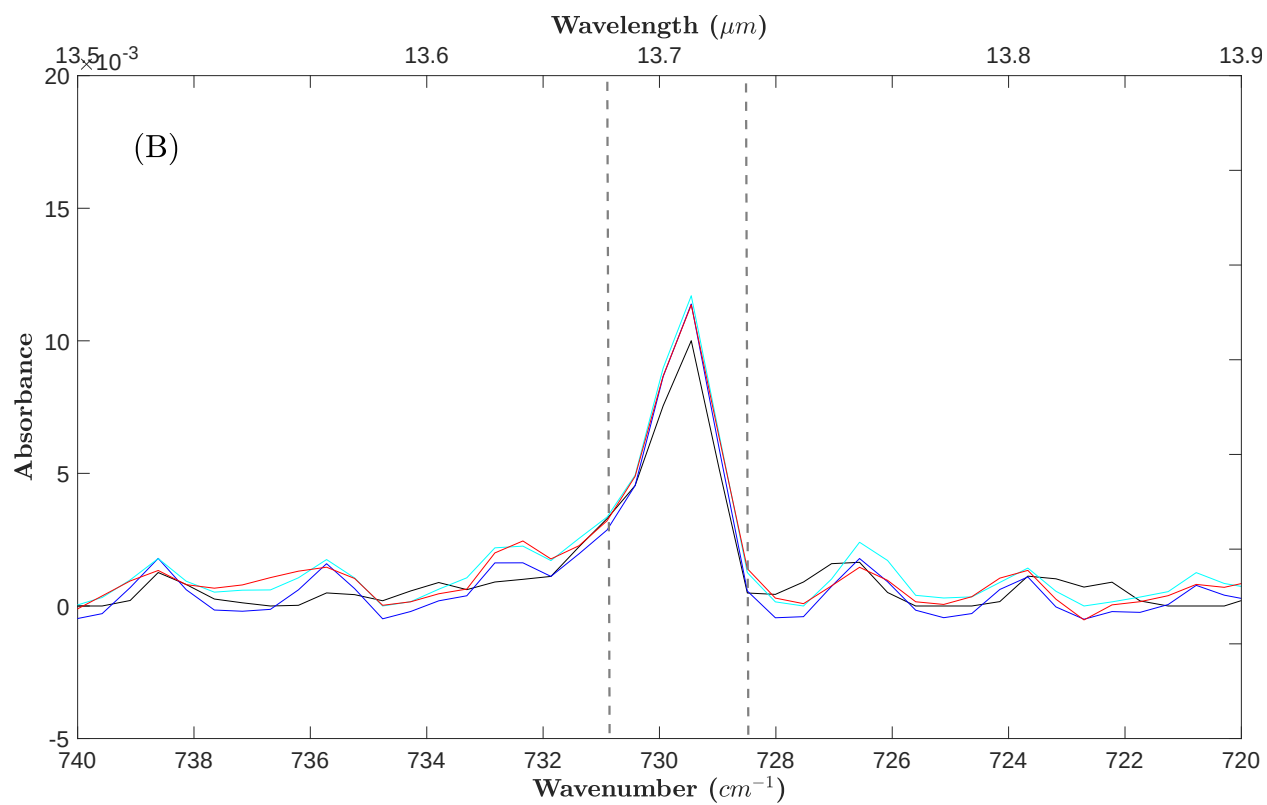
Fig. 9. $[CH_4]_0$ = 1%. Main absorption bands of (A) NH_3 (930 cm^{-1} and 960 cm^{-1} doublet), (B) C_2H_2 (729.25 cm^{-1}), (C) HCN (713 cm^{-1}), (D) C_2H_4 (949.55 cm^{-1}). The color code is the same as in Figure 6. The vertical dashed gray lines correspond to the integration band used for the density calculations on either side of the absorption peaks.

10% CH$_4$
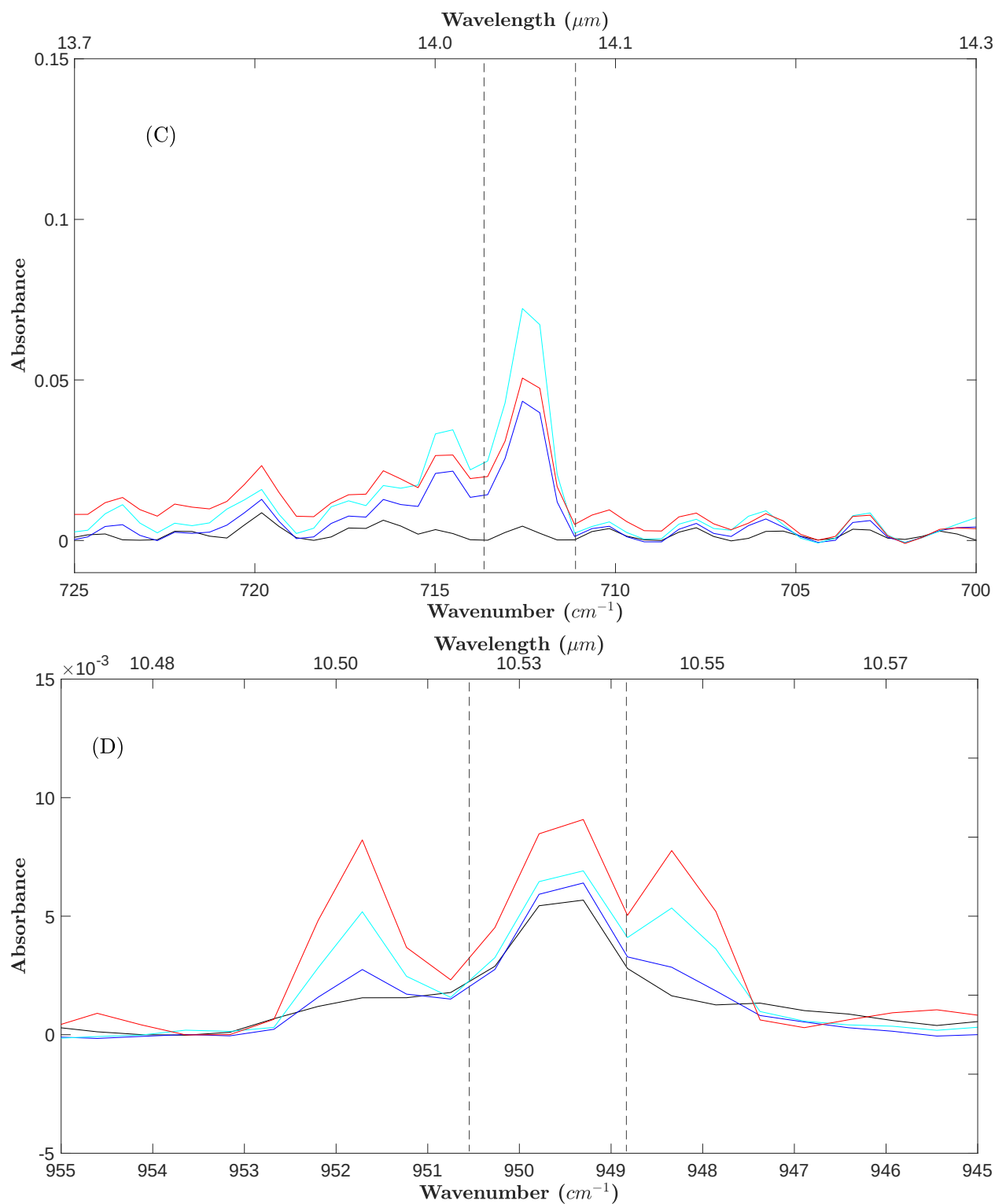
Fig. 10. [CH$_4$]$_0$ = 10%. Main absorption bands of (A) NH$_3$ (930 cm^{-1} and 960 cm^{-1} doublet), (B) C$_2$H$_2$ (729.25 cm^{-1}), (C) HCN (713 cm^{-1}), (D) C$_2$H$_4$ (949.55 cm^{-1}). The color code is the same as in Figure 7. The vertical dashed gray lines correspond to the integration band used for the density calculations on either side of the absorption peaks.
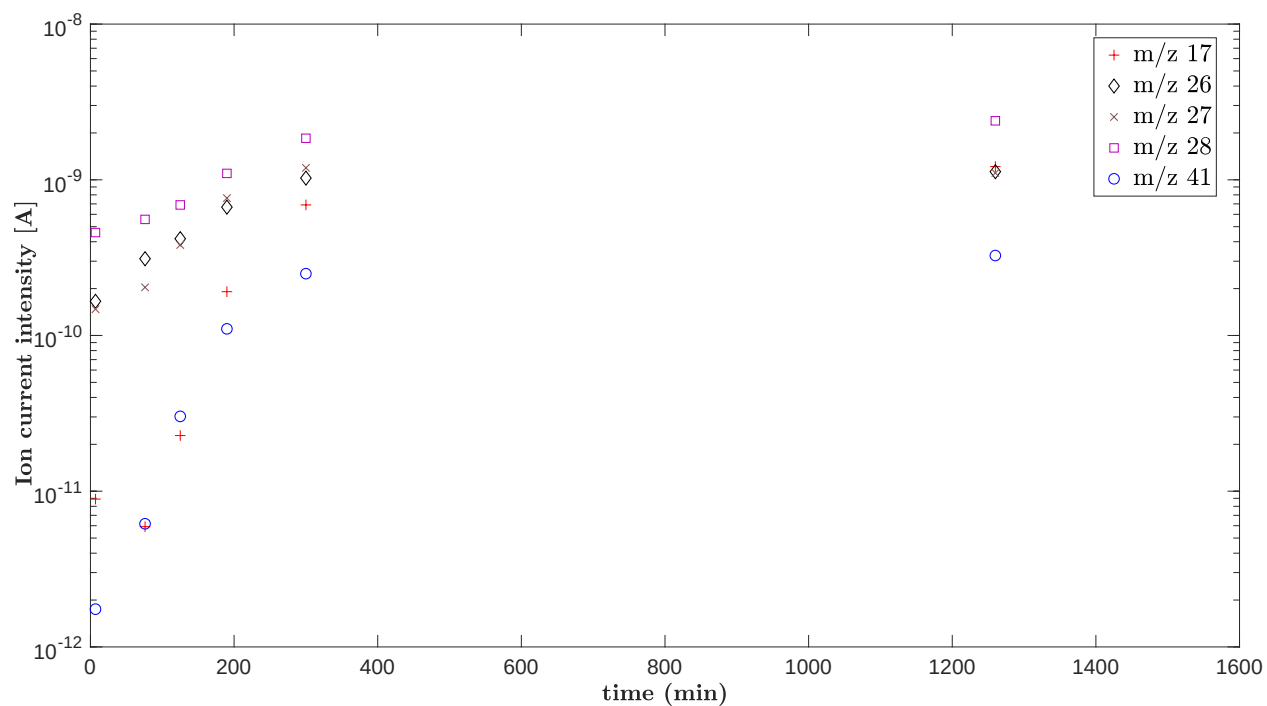
Fig. 11. Evolution of the intensities (same time scale as Figure 3) of selected species, NH_3 (m/z 17), C_2H_2 (m/z 26), HCN (m/z 27), C_2H_4 (m/z 28) and CH_3CN (m/z 41) over time.

Selected species	Fundamental frequency[1]	Main peak (cm^{-1})	FWHM (cm^{-1})	Integrated absorption cross-section σ (cm^2.molecule^{-1})
Ammonia	υ_2	965	± 4.0	4.04 × 10^{-18}
Acetylene	υ_5	729.25	± 1.25	1.92 × 10^{-16}
Hydrogen Cyanide	υ_2	712.3	± 1.2	4.09 × 10^{-18}
Ethylene	υ_7	949.5	± 1.0	2.43 × 10^{-17}

Table 3. IR peak locations, fundamental frequencies and integrated wavenumber ranges, absorption cross-sections (cm^2.molecule^{-1}) for each selected volatile, as analyzed in both methane conditions. For the calculation results (derived from Equ. 6), see the following Tables 4-5. [1]Sharpe et al., 2004 and

http://vpl.astro.washington.edu/spectra/allmoleculeslist.htm

Time/Species	NH_3 (cm^{-3})			C_2H_2 (cm^{-3})			HCN (cm^{-3})			C_2H_4 (cm^{-3})		
T_1	5.6×10^{11}	2.8×10^{13}	1.4×10^{14}	2.1×10^{12}	2.4×10^{12}	1.4×10^{12}	4.0×10^{12}	2.5×10^{13}	-	-	-	-
mean	5.6×10^{13}			2.0×10^{12}			9.7×10^{12}			-		
T_2	7.0×10^{13}	3.1×10^{14}	4.0×10^{14}	3.1×10^{12}	3.0×10^{12}	2.8×10^{12}	1.3×10^{13}	8.3×10^{13}	1.4×10^{13}	-	-	-
mean	2.6×10^{14}			3.0×10^{12}			3.7×10^{13}			-		
T_3	1.6×10^{14}	5.6×10^{14}	6.1×10^{14}	3.1×10^{12}	2.9×10^{12}	3.2×10^{12}	1.7×10^{13}	1.2×10^{14}	2.8×10^{13}	-	-	-
mean	4.4×10^{14}			3.1×10^{12}			5.5×10^{13}			-		
T_4	5.2×10^{14}	5.3×10^{14}	8.2×10^{14}	3.7×10^{12}	3.0×10^{12}	3.4×10^{12}	2.1×10^{14}	1.8×10^{14}	1.7×10^{14}	-	-	-
mean	6.2×10^{14}			3.4×10^{12}			1.9×10^{14}			-		
T_5	9.6×10^{14}	8.6×10^{14}	1.3×10^{15}	4.4×10^{12}	3.1×10^{12}	4.5×10^{12}	2.0×10^{14}	1.5×10^{14}	1.7×10^{14}	-	-	-
mean	1.0×10^{15}			4.0×10^{12}			1.7×10^{14}			-		
T_6	9.6×10^{14}	1.3×10^{15}	1.1×10^{15}	3.4×10^{12}	3.6×10^{12}	2.6×10^{12}	1.7×10^{14}	1.6×10^{14}	1.1×10^{14}	-	-	-
mean	1.1×10^{15}			3.2×10^{12}			1.5×10^{14}			-		

Table 4. Calculated molecular densities from IR absorption at $[CH_4]_0$ = 1%, for three different data sets. T_{1-6} correspond to measurements done at approximately 30 min (-130ºC), 60 min (-85ºC), 120 min (-70ºC), 180 min (-41ºC), 1200 min (+22ºC) and 1440 min (+22ºC), respectively. Each column corresponds to one experiment. Number density calculations are performed with the integrated absorption cross-section of the ExoMol or Hitran databases at the resolution of our experimental spectra (see Table 3). Blank boxes indicate the absence of the species where no number density was derived.

Time/Species	NH_3 (cm^{-3})		C_2H_2 (cm^{-3})		HCN (cm^{-3})		C_2H_4 (cm^{-3})	
T_1	-	-	2.0×10^{13}	2.2×10^{13}	-	-	8.3×10^{12}	5.5×10^{12}
mean	$-$		2.1×10^{13}		$-$		6.9×10^{12}	
T_2	3.5×10^{14}	-	2.9×10^{13}	3.0×10^{13}	6.5×10^{14}	4.5×10^{15}	1.4×10^{13}	3.3×10^{12}
mean	3.5×10^{14}		3.0×10^{13}		2.6×10^{15}		8.7×10^{12}	
T_3	8.6×10^{14}	1.6×10^{15}	3.5×10^{13}	4.9×10^{13}	1.1×10^{15}	2.4×10^{15}	1.1×10^{13}	5.9×10^{13}
mean	1.2×10^{15}		4.2×10^{13}		1.8×10^{15}		3.5×10^{13}	
T_4	2.3×10^{15}	5.0×10^{14}	4.1×10^{13}	3.2×10^{13}	8.5×10^{14}	1.5×10^{15}	2.2×10^{13}	4.3×10^{13}
mean	1.4×10^{15}		3.7×10^{13}		1.2×10^{15}		3.3×10^{13}	

Table 5. Calculated molecular densities from IR absorption at $[CH_4]_0$ = 10%, for two different data sets. T_{1-4} correspond to measurements done at approximately 7 min (-130ºC), 125 min (-66ºC), 190 min (-44ºC) and 21h (+22ºC), respectively. Each column corresponds to one experiment. Number density calculations are performed with the integrated absorption cross-section of the ExoMol or Hitran databases at the resolution of our experimental spectra (see Table 3). Blank boxes indicate the absence of the species where no number density was derived.